

Multicomponent Resonant Nanostructures: Plasmonic and Photothermal Effects

Vadim Zakomirnyi



Department of Theoretical Chemistry and Biology
School of Engineering Sciences in Chemistry, Biotechnology and Health,
Royal Institute of Technology
Stockholm, Sweden 2019

© Vadim Zakomirnyi, 2019
ISBN 978-91-7873-395-8
TRITA-CBH-FOU-2019:69
Printed by Universitetsservice US AB,
Stockholm, Sweden, 2019

Abstract

In recent decades, plasmonic nanoparticles have attracted considerable attention due to their ability to localize electromagnetic energy at a scale much smaller than the wavelength of optical radiation. The study of optical plasmon waveguides (OPWs) in the form of chains of nanoparticles is important for modern photonics. However, the widespread use of OPWs is limited due to the suppression of the resonance properties of classical plasmon materials under laser irradiation. The study of the influence of nanoparticle heating on the optical properties of waveguides and the search for new materials capable of stable functioning at high temperatures is an important task.

In this thesis, the processes occurring during heating of plasmon nanoparticles and OPWs are studied. For this purpose, a model was developed that takes into account the heat transfer between the particles of an OPW and the environment. The calculations used temperature-dependent optical constants. As one of possible ways to avoid thermal destabilization of plasmon resonances, new materials for OPWs formed by nanoparticles were proposed. I show that titanium nitride is a promising thermally stable material, that might be useful for manufacturing of OPWs and that works in high intensity laser radiation.

Another hot topic at present is the study of periodic structures of resonant nanoparticles. Periodic arrays of nanoparticles have a unique feature: the manifestation of collective modes, which are formed due to the hybridization of a localized surface plasmon resonance or a Mie resonance and the Rayleigh lattice anomaly. Such a pronounced hybridization leads to the appearance of narrow surface lattice resonances, the quality factor of which is hundreds of times higher than the quality factor of the localized surface plasmon resonance alone. Structures that can support not only electric, but also magnetic dipole resonances becomes extremely important for modern photonics on chip systems. An example of a material of such particles is silicon. Using the method of generalized coupled dipoles, I studied the optical response of arrays of silicon nanoparticles. It is shown that under certain conditions, selective hybridization of only one of the dipole moments with the Rayleigh anomaly occurs.

To analyze optical properties of intermediate sized particles with $N = 10^3 - 10^5$ atoms and diameter of particle $d < 12$ nm an atomistic approach, where the polarizabilities can be obtained from the atoms of the particle, could fill an important gap in the description of nanoparticle plasmons between the quantum and classical extremes. For this purpose I introduced an extended discrete interaction model where every atom makes a difference in the formation optical properties of nanoparticles within this size range. In this range are first principal approaches not applicable due to the high number of atoms and classical models based on bulk material dielectric constants are not available due to high influence from

quantum size effects and corrections to the dielectric constant. To parametrize this semi-empirical model I proposed a method based on the concept of plasmon length. To evaluate the accuracy of the model, I performed calculations of optical properties of nanoparticles with different shapes: regular nanospheres, nanocubes and nanorods. Subsequently, the model was used to calculate hollow nanoparticles (nano-bubbles).

List of goals of current research:

1. Investigate the influence of limitation caused by thermal effects arising from the excitation of an optical plasmon waveguide in the form of a linear chain of spherical nanoparticles in high energy laser radiation.
2. Show the effect of heating and subsequent melting of the first irradiated particle in the chain on the efficiency of the transmission of an optical signal through an optical plasmon waveguide.
3. Investigate the possibility of using titanium nitride as an alternative material with high thermal stability for optical plasmonic waveguides from spherical and spheroidal nanoparticles.
4. Obtain information on the effect of imperfections (various types of defects) that may appear in two-dimensional arrays of silicon nanoparticles where collective optical effects associated with the manifestation of high-quality lattice resonances.
5. Develop a model for describing the optical properties of plasmon nanoparticles based on a discrete atomic interaction model using a plasmon length based parametrization.
6. Demonstrate the size, shape and aspect ratio dependence of surface plasmon resonances for small (2 – 12 nm in diameter) silver spherical- and cubical-clusters and nanorods.
7. Demonstrate the resonance properties of hollow nanoparticles and compare classic electrodynamics simulations of optical properties of small nanoparticles using Mie theory with my discrete atomic interaction model.

Preface

The work presented in this thesis has been carried out at the Department of Theoretical Chemistry and Biology, Royal Institute of Technology, Stockholm, Sweden, and at the Institute of Nanotechnology, Spectroscopy and Quantum Chemistry, Siberian Federal University (SibFU), Krasnoyarsk, Russia in the framework of the double doctorate cooperation between KTH and SibFU.

List of papers included in the Thesis

Paper I V. S. Gerasimov, A. E. Ershov, S. V. Karpov, A. P. Gavriluk, V. I. Zakomirnyi, I. L. Rasskazov, H. Ågren, S. P. Polyutov, "Thermal effects in systems of colloidal plasmonic nanoparticles in high-intensity pulsed laser fields", *Optical Materials Express*, **7**(2), 555 (2017).

Paper II V. I. Zakomirnyi, I. L. Rasskazov, V. S. Gerasimov, A. E. Ershov, S. P. Polyutov, S. V. Karpov, H. Ågren, "Titanium nitride nanoparticles as an alternative platform for plasmonic waveguides in the visible and telecommunication wavelength ranges", *Photonics and Nanostructures - Fundamentals and Applications* **30**, 50-56 (2018).

Paper III V. I. Zakomirnyi, S. V. Karpov, H. Ågren, I. L. Rasskazov, "Collective lattice resonances in disordered and quasi-random all-dielectric metasurfaces", *Journal of the Optical Society of America B* **36**(7), E21 (2019).

Paper IV A. D. Utyushev, I. L. Isaev, V. S. Gerasimov, A. E. Ershov, V. I. Zakomirnyi, I. L. Rasskazov, S. P. Polyutov, H. Ågren, S. V. Karpov, "Engineering novel tunable optical high-Q nanoparticle array filters for a wide range of wavelengths", submitted in *Optics Express* (2019).

Paper V V. I. Zakomirnyi, Z. Rinkevicius, G. V. Baryshnikov, L. K. Sørensen, H. Ågren, "The Extended Discrete Interaction Model: Plasmonic Excitations of Silver Nanoparticles", accepted in *The Journal of Physical Chemistry C* (2019).

Paper VI V. I. Zakomirnyi, A. E. Ershov, V. S. Gerasimov, S. V. Karpov, H. Ågren, I. L. Rasskazov, "Collective lattice resonances in arrays of dielectric nanoparticles: a matter of size", *Optics Letters* **44**(23), 5743–5746 (2019).

Paper VII V. I. Zakomirnyi, I. L. Rasskazov, L. K. Sørensen, P. S. Carney, Z. Rinkevicius, H. Ågren, "Plasmonic nano-bubbles: atomistic discrete interaction versus classic electrodynamics models", manuscript (2019).

Comments on my contributions to the papers included

- I was responsible for a part of the simulations and participated in discussions of theory and results of **Papers I, IV, VII**.
- I was responsible for the major part of calculations and simulations in **Papers II, III, V and VI**. I also contributed to figures preparation, discussion of the results and writing of the manuscript.

List of other papers not included in the Thesis

Paper I V. I. Zakomirnyi, I. L. Rasskazov, S. V. Karpov, S. P. Polyutov, "New ideally absorbing Au plasmonic nanostructures for biomedical applications", *Journal of Quantitative Spectroscopy and Radiative Transfer* **187**, 54-61 (2017).

Paper II A. E. Ershov, V. S. Gerasimov, A. P. Gavriluk, S. V. Karpov, V. I. Zakomirnyi, I. L. Rasskazov, S. P. Polyutov, "Thermal limiting effects in optical plasmonic waveguides", *Journal of Quantitative Spectroscopy and Radiative Transfer* **191**, 1-6 (2017).

Paper III V. I. Zakomirnyi, I. L. Rasskazov, V. S. Gerasimov, A. E. Ershov, S. P. Polyutov, S. V. Karpov, "Refractory titanium nitride two-dimensional structures with extremely narrow surface lattice resonances at telecommunication wavelengths", *Applied Physics Letters* **111**(12), 123107 (2017).

Acknowledgments

I would like to express my deep gratitude to Professor Hans Ågren and Professor Zilvinas Rinkevicius, my research supervisors, for their patient guidance, enthusiastic encouragement and useful critiques of this research work. I wish to thank Professor Sergey V. Karpov, who was my first supervisor and who provided me an opportunity to participate in ongoing research on plasmonics project in the group at Kirensky Institute of Physics (Krasnoyarsk, Russia). Thanks to my colleague Dr. Lasse Kragh Sørensen for the fantastic patience and great participation in my work. Many thanks to Dr. Sergey P. Polyutov for great contribution in my scientific career and to the Siberian Federal University (Krasnoyarsk, Russia) for ample institutional resources. The Scholarship of President of Russian Federation for education abroad is gratefully acknowledged for financial support.

I truly appreciate lectures given by Prof. Olav Vahtras, Prof. Yaoquan Tu, Prof. Mårten Ahlquist and Dr. Victor Kimberg. Special thanks are given to Prof. Faris Gel'mukhanov for some nice talks and discussions together, and Prof. Lars Thylén for his interest in my work and inspiring discussions about future of plasmonics and photonics.

The administrative staff at Theochem Department, in particular Nina Bauer, is acknowledged for all administrative help. Special thanks to Nina for her help with my visa and for teaching me how to understand Swedish humor.

My special appreciate to my colleagues and friends for their support in providing relevant assistant and help to complete my study. Thanks to Valeriy Gerasimov, Alexander Ershov, Karan Ahmadzadeh, Iulia-Emilia Brumboiu, Haofan Sun, Lucia Labrador Paez, Michal Biler, Nicolas Rolland, Nina Ignatova, Qingyun Liu, Rafael Carvalho Couto and Vinícius Vaz da Cruz. Special thanks to Glib Baryshnikov for tons of coffee and endless discussions about chemistry.

No one was more important to me in the implementation of this project than Ilia Rasskazov. Thank you for valuable guidance, timely suggestions and support throughout my research project work.

Last but not least, I want to thank my wife Anna, whose love and care support me and provide endless inspiration.

Vadim I. Zakomirnyi

Stockholm, 2019-12-19

Contents

1	Introduction	1
2	Thermal and optical effects in plasmonic nanoparticle waveguides	5
2.1	Model	6
2.1.1	Dipole approximation	6
2.1.2	Optical properties of melted nanoparticles	6
2.1.3	Thermodynamic properties of nanoparticles	7
2.1.4	Thermodynamic properties of optical plasmonic waveguides	10
2.1.5	Transmission and dispersion properties of optical plasmonic waveguides	11
2.2	Results	13
2.2.1	Thermal and optical properties of optical plasmonic waveguides from silver nanoparticles	13
2.2.2	Optical properties of optical plasmonic waveguides from titanium ni- tride nanoparticles	17
2.3	Conclusions for Chapter 2	21
3	Collective effects in structures of resonant nanoparticles	23
3.1	Model	23
3.1.1	Extended coupled dipole approximation	23
3.1.2	Types of imperfections in arrays on silicon nanoparticles	25
3.2	Results	27
3.2.1	Periodic arrays of silicon nanoparticles	27

3.2.2	Arrays of silicon nanoparticles with imperfections	29
3.2.3	Finite size effects in arrays of silicon nanoparticles	33
3.2.4	Optical filters based on arrays of plasmonic nanoparticles	35
3.3	Conclusions for Chapter 3	37
4	Extended discrete interaction model for calculating optical properties of plasmonic nanoparticles	39
4.1	Model	40
4.1.1	Extended discrete interaction model	40
4.1.2	Parametrization of extended discrete interaction model for silver . . .	43
4.2	Results	48
4.2.1	Polarizability of spherical silver nanoparticles	48
4.2.2	Polarizability of silver nanoparticles with complicated geometry: nanocubes and nanorods	51
4.2.3	Plasmon resonances of hollow nanoparticles	53
4.2.4	Polarizability of hollow nanoparticles	55
4.3	Conclusions for Chapter 4	56
5	Summary	57
	Bibliography	59

List of abbreviations

NP - Nanoparticle

DA - Dipole Approximation

OPW - Optical Plasmonic Waveguide

CLR - Collective Lattice Resonance

IR - Infrared (wavelength region)

ED - Electric Dipole

MD - Magnetic Dipole

FDTD - Finite-Difference Time-Domain

SPP - Surface Plasmon Polariton

SPR - Surface Plasmon Resonance

TLSPR - SPR localized along the transverse axis (short axis in spheroids)

LLSPR - SPR localized along the longitudinal axis (long axis in spheroids)

DIM - Discrete Interaction Model

ex-DIM - Extended DIM

cd-DIM - Coordination Dependent DIM

Chapter 1

Introduction

Currently, plasmonics constitutes one of the most interesting areas of development in photonics. With "plasmonics", we, of course, mean the manifestation of the so-called plasmon resonances which are produced by group oscillations of conduction electrons that lead to an increase in the absorption of electromagnetic radiation at certain wavelengths. The plasmon resonance in small nanoparticles strongly depends on their geometric shape, size, and material. Homogeneous spherical nanoparticles of silver and gold are well-studied objects in nanoplasmonics. However, due to technical limitations associated with the complexity of the experimental manufacturing of silver and gold nanoparticles, attempts have been made to use alternative plasmon materials. One looks for materials that can have advantages compared to the classical materials in terms of, for example, increased heat resistance and chemical stability. Obviously, one can find advantages in combining various materials, for example, for the manufacturing of nanoparticles with a core-shell structure, where the shell performs a protective function. In addition to using various materials for nanoparticles, the influence of the geometry of nanoparticles is of interest. It is well known that the appearance of additional plasmon resonances is observed for nanoparticles in the form of prolate or oblate spheroids. The nature of such resonances are rather well studied theoretically and these resonance particles have been repeatedly used in various applications. There are also studies of more complex geometries of nanoparticles, such as pyramids, cubes, nanostars, nanorods, nanobubbles.

It is worthwhile to consider the reasons for the interest in plasmonic nanoparticles and structures of plasmonic nanoparticles from the point of view of possible applications in modern nanophotonics. The potential applications of plasmonic nanoparticles are based on their unique feature of supporting plasmon resonances that enhance the local field near the nanoparticle. An electromagnetic field near a nanoparticle at a plasmon resonance

wavelength can be two or more orders of magnitude stronger than at other frequencies. In the simplest case of a single nanoparticle in laser illumination, this inevitably leads to heating of the nanoparticle and possibly also to a change in their phase state, in other words, melting. If such a nanoparticle is placed near a living cell, the super hot nanoparticle can burn the cell membrane and destroy the cell. This technique is known and widely used in so-called plasmon photothermal therapy of cancer cells. In the case of a pair of closely spaced nanoparticles, the field between them can be enhanced by more than four orders of magnitude. By placing the molecule there, and controlling the external radiation, one can "highlight" the molecule and obtain an amplified Raman spectrum. Chains of equidistant nanoparticles of various shapes attract attention of researchers due to the ability to transmit plasmon excitation, which is nothing but a plasmon waveguide. Despite the obvious advantages of using such waveguides in modern nanophotonics, there are a number of effects that limit the widespread use of such waveguides and which is the source of much current research.

In recent years, two-dimensional arrays of nanoparticles have begun to attract great attention. Periodic arrays of plasmonic nanoparticles have a unique feature: the manifestation of collective modes, which are formed due to the hybridization of surface plasmon resonances and the Wood-Rayleigh lattice anomalies. This hybridization leads to the appearance of a narrow collective lattice resonance with a quality factor many times higher than the quality factor of the surface plasmon resonance. Collective lattice resonances have attracted attention over the past decade, starting with pioneering theoretical research [1–3] and applied experimental work in vibrational spectroscopy [4], ultra-narrowband absorption [5], sensors [6, 7], lasers [8], and enhanced fluorescence [9, 10]. Collective lattice resonances have been studied in a wide range of periodic nanostructures with various types of unit cells: single [11] or double layers [12] nanodisks, cylinders and nanoshells [13], nanoparticle dimers [14, 15], complex nanoparticles [16], split ring resonators [17], oligomers [18] and other complex configurations [19–22]. The position and shape of a collective plasmon resonance is affected not only by the size, material, and shape of the single nanoparticles, but also by the geometry of the array itself. Thus, an ordered equidistant lattice of nanoparticles will differ from the structure in which the distances between the particles differ along the X and Y axis, or from the structure in which the nanoparticles are ordered in something resembling a honeycomb and other geometries. Currently, attention is focused on lattices from classical plasmon materials [11, 23–25] (Au and Ag) with an surface plasmon resonance peak of individual nanoparticles located in the visible or near infrared region.

Although nanoplasmonics since long has constituted a research branch that has received strong attention as a versatile nanotechnology and by now turned into mature research with significant applications in areas like bioimaging, photonics and energy harvesting, there is

still a lag between experiment and theoretical capability to design nanostructures with particular plasmonic properties. Among a number of classical models, Mie theory has been instrumental in predicting light scattering and plasmonic resonances in metallic nanoparticles. Since Mie theory relies on the concept of a dielectric constant it is, however, restricted to a size comprising larger nanoparticles where the classical bulk dielectric constant remains valid and frequency ranges where experimental results are available. At the other hand, pure quantum approaches, like time-dependent density functional theory, are applicable only for the very small particles. This leaves the 1–15 nm size region unattainable by either classical (n.b. Mie) and quantum theory, which is unfortunate considering the wide applicability of small plasmonic nanoparticles within that size range, e.g. for cell imaging [26, 27].

The first part of my thesis concerns the study of the interaction of metal nanoparticles with laser radiation as one of the main directions in nanoplasmonics. My work touches on many possible applications in fields such as nanosensors, biomedicine [28–45], biotechnology, laser excitation of plasmon polaritons in waveguides from chains of plasmon nanoparticles, photochromic reactions induced by laser excitation of resonant domains in disordered colloidal aggregates of nanoparticles and various nonlinear optical processes. Monographs and reviews [46–50] cover a large number of recent works and applications. There are a number of earlier works that form the basis for the research development reported in my thesis: In [51–53] studies of heating nanoparticles with laser radiation were presented and in [54–56] the effects of pulsed laser radiation on aggregates of plasmon nanoparticles have been analyzed taking into account the effects of the melting of nanoparticles. However, the most part of current research does not take into account the change in optical properties with the change in temperature of the nanoparticles, and vice versa. Thus, there is interest in developing thermodynamic models that take into account heat transfer between nanoparticles inside the optical plasmonic waveguide, the environment, and the substrate, and that also take into account the temperature dependencies of the optical properties of the nanoparticles.

Also, I thoroughly addressed the problem of diffractive behavior of electric dipole and magnetic dipole resonances in imperfect arrays of spherical silicon nanoparticles. A comprehensive analysis of various types of disorder revealed the effect on the hybridization scenario of the electric dipole and magnetic dipole modes with lattice modes. Among other things, it is not obvious how collective lattice resonances in arrays of finite sizes of dielectric nanoparticles with strong electric dipole and magnetic dipole resonances differ from collective lattice resonances in infinite arrays. Thus, due to strong self-interactions between the electric dipole and magnetic dipole modes, I studied the problem of the validity of the infinite array approximation when working with collective lattice resonances in arrays of nanoparticles with electric dipole and magnetic dipole resonances.

Motivated by the wide applicability of small plasmonic nanoparticles and by the need to

find a "bridge" in the length gap between classical and quantum theory to describe plasmon generation, I introduced in the last part of my thesis an extended discrete interaction model to simulate optical properties of nanoparticles with different geometry in size range between 1 and 15 nm.

Despite years of research efforts in nanoplasmonic, the area remains wide open for further development of theory and modelling with ramifications for applications in many technological areas, like biomiaging, photonics, energy harvesting and other current front-edge technologies. It is my hope that my thesis makes a contribution to that endeavour.

Chapter 2

Thermal and optical effects in plasmonic nanoparticle waveguides

Changes in the optical properties of the particle material due to melting is an important factor in the process of interaction of laser radiation with nanoparticles (NPs). This is due to the fact that with an increase in the temperature of the NPs, the intensity of phonon vibrations increases. As a result of this, the frequency of electron scattering by phonons increases, which leads to an increase in the electron relaxation constant (above the Debye electron relaxation temperature it increases in proportion to the temperature) [57]. During melting, the gradual destruction of the periodic structure in the crystal leads to the scattering of conduction electrons by lattice defects (mainly vacancies and dislocations) up to complete amorphization. The melting process is accompanied by a sharp increase in relaxation constants. In addition to phonons, the contribution to the electronic relaxation of a metal is determined by the scattering of electrons by point defects, dislocations, particle boundaries, and electrons [57]. It was shown that heating of nanoparticles and their subsequent melting significantly affects their resonance properties. A theoretical approach that describes the heat transfer between nanoparticles and the environment [54, 56, 58] is also applicable in the case of a single laser pulse with a duration much shorter than the time to establish a thermodynamic equilibrium. However, such models do not take into account the effect of the substrate, which can play a crucial role of a cooling device.

2.1 Model

2.1.1 Dipole approximation

The electrodynamics part of plasmonic model is based on the dipole approximation [59], which allows us to calculate the electromagnetic interaction between NP and the incident radiation. Let us consider an NP in a medium with a dielectric constant ε_h which is irradiated by a plane electromagnetic wave $\mathbf{E}(\mathbf{r}) = \mathbf{E}_0 \exp(i\mathbf{k} \cdot \mathbf{r})$. Here $\mathbf{E}(\mathbf{r})$ is electric field at location \mathbf{r} , $|\mathbf{k}| = 2\pi\sqrt{\varepsilon_h}/\lambda$ is a wave vector, λ is a wavelength, \mathbf{E}_0 is amplitude of the electric component of the electromagnetic field. In a general case, the dipole moment \mathbf{d} induced at the NP can be described by the following equation [59]:

$$\mathbf{d} = \varepsilon_h \alpha^e \mathbf{E}(\mathbf{r}), \quad (2.1)$$

where α^e is the electric dipole polarizability of the NP [59, 60]:

$$\frac{1}{\alpha^e} = \frac{1}{\alpha^{(0)}} - \frac{i}{6\pi} |\mathbf{k}|^3, \quad (2.2)$$

where $\alpha^{(0)}$ is a quasistatic polarizability of the NP [61]:

$$\alpha^{(0)} = 4\pi R^3 \frac{\varepsilon - \varepsilon_h}{\varepsilon + 2\varepsilon_h}. \quad (2.3)$$

Here R is a radius and ε is the dielectric permittivity of the NP.

2.1.2 Optical properties of melted nanoparticles

When the NP absorbs electromagnetic radiation, it heats up until it is completely melted (liquid). This factor may be accompanied by cyclically repeated rises and drops of temperature of resonantly excited NP. These cycles appear due to the termination of the resonant interaction between incident optical radiation and liquid of particles. Therefore, it is necessary to take into account the fact that NP also can be in a molten state. In other words, NP can be represented as layered nanoparticle with a solid core and a liquid shell. In this case, we can apply the concept of a nanoshell to such NP, the materials of the core and shell of which are the same, but in different aggregate states. The quasistatic polarizability for the n -th NPs from eq. (2.3) will be changed in following way [62]:

$$\alpha_n^{(0)} = 4\pi R_n^3 \frac{(\varepsilon_n^l - \varepsilon_h)(\varepsilon_n^s + 2\varepsilon_n^l) + f_n(\varepsilon_n^s - \varepsilon_n^l)(\varepsilon_h + 2\varepsilon_n^l)}{(\varepsilon_n^l + 2\varepsilon_h)(\varepsilon_n^s + 2\varepsilon_n^l) + 2f_n(\varepsilon_n^s - \varepsilon_n^l)(\varepsilon_n^l - \varepsilon_h)}, \quad (2.4)$$

where ε_n^s and ε_n^l are the dielectric constants of the particle material in the solid and liquid state, respectively. The value f_n is the fraction of the solid part of the whole nanoparticle. Equation (2.4) also takes into account the cases when the NP is a complete liquid ($f_n = 0$) or a complete solid ($f_n = 1$). Due to high surface tension forces, the NPs will keep their spherical shape even when they are complete liquids, which makes eq. (2.4) applicable for any values of f_n . The dielectric constants ε_n^s and ε_n^l also take into account finite size effects:

$$\varepsilon_n^{s,l} \rightarrow \varepsilon_{tab}^{s,l} + \frac{\omega_p^2}{\omega^2 + i\gamma_{bulk}\omega} - \frac{\omega_p^2}{\omega^2 + i\gamma_{fin}\omega}, \quad (2.5)$$

where $\omega = 2\pi c/\lambda$ is the frequency of incident radiation, ε_{tab}^s and ε_{tab}^l are the tabulated experimental values of the dielectric constant for solid bulk material at temperature 300 K [63] and dielectric constant for fully melted liquid material [64] respectively, ω_p is a plasma frequency, γ_{bulk} and γ_{fin} are relaxation constants [65]:

$$\gamma_{fin} = \gamma_{bulk} + A_L \frac{v_F}{L_{eff}}, \quad (2.6)$$

where v_F is the Fermi velocity; L_{eff} is the electron effective mean free path [66], and A_L is a dimensionless parameter, which is close to 1 in our studied cases [62]. It should be noticed that γ_{bulk} is a parameter depending on the temperature T_{ion} , and can be approximated by the following expression [57]:

$$\gamma_{bulk}(T_{ion}) = bT + c, \quad (2.7)$$

where b and c are coefficients obtained from a linear approximation of experimental data [67].

2.1.3 Thermodynamic properties of nanoparticles

The absorption of laser radiation leads primarily to the heating of conductivity electrons (electronic subsystem) in nanoparticles and their crystal lattice (ionic subsystem). The changes in temperature of the electronic subsystem T_n^{el} , caused by the absorption of electromagnetic energy and heat transfer with the ionic subsystem (with temperature T_n^{ion}), is described by the equation [68, 69]:

$$C_n^{\text{el}} \frac{dT_n^{\text{el}}}{dt} = -g \left[T_n^{\text{el}} - T_n^{\text{ion}} \right] + \frac{W_n}{V_n}, \quad (2.8)$$

where C_n^{el} is the volumetric heat capacity of the electronic subsystems: $C_n^{\text{el}} = 68 T_n^{\text{ion}} \text{ J} \cdot \text{m}^{-3} \cdot \text{K}^{-1}$, T_n^{ion} is temperature of the ionic subsystem, V_n is particle volume, $g = 4 \cdot 10^{16} \text{ J} \cdot \text{m}^{-3} \cdot \text{K}^{-1} \cdot \text{s}^{-1}$ is the temperature-independent energy exchange rate between the electron and ion subsystems, that should be higher than the Debye temperature [70–72], W_n is the power of energy absorbed by the nanoparticle. In the dipole approximation, W_n is defined by the following expression [56, 73]:

$$W_n = \frac{\omega |\mathbf{d}_n|^2}{2\varepsilon_h} \text{Im} \left(\frac{1}{\alpha_n^*} \right). \quad (2.9)$$

where ω is the frequency of incident radiation, \mathbf{d}_n is a vector of the dipole moment of the n -th NP, asterisk $*$ means complex conjugate value of the polarizability from eq. (2.2).

The changes in the temperature of the ionic subsystem T_n^{ion} of the NP is mainly determined by the heat exchange between the electronic subsystem and the environment. Taking into account the solid-to-liquid phase transition in NPs, we use the equation for the thermal energy of the NPs lattice Q_n^{ion} instead of the T^{ion} :

$$\frac{dQ_n^{\text{ion}}}{dt} = g V_n \left[T_n^{\text{el}} - T_n^{\text{ion}} \right] + q_n^l V_n, \quad (2.10)$$

where q_n^l is a heat flow per unit volume explaining heat losses [68]:

$$q_n^l = -\frac{3}{2R_n} (T_n^{\text{ion}} - T_0) \sqrt{\frac{\chi_m c_{m0} \rho_m}{t}}, \quad (2.11)$$

where χ_m is thermal conductivity of interparticle medium, c_{m0} is heat capacity, ρ_m is density, t is time of a laser pulse.

The temperature of the ionic subsystem, taking into account the melting process, is expressed in terms of Q_n^{ion} :

$$T_n^{\text{ion}} = \frac{Q_n^{\text{ion}}}{C_n V_n} H(Q_n^{(1)} - Q_n^{\text{ion}}) + \frac{Q_n^{\text{ion}} - Q_n^{(2)}}{C_n V_n} H(Q_n^{\text{ion}} - Q_n^{(2)}) + T^{\text{m}}(R_n) H(Q_n^{\text{ion}} - Q_n^{(1)}), \quad (2.12)$$

where $Q_n^{(1)}$ and $Q_n^{(2)}$ are the thermal energies of the particle corresponding to the beginning and to the end of melting process respectively, C_n is the volumetric heat capacity of the

ionic subsystem of NPs, $T^m(R_n)$ is the melting point depending on particle size [74], $H(x)$ is the Heaviside function.

The temperature of the ionic subsystem of a nanoparticle during melting might also be determined as follows [56]:

$$T_n^{\text{ion}} = \begin{cases} \frac{Q_n^{\text{ion}}}{C_n^{\text{ion}} V_n}, & \text{where } Q_n^{\text{ion}} < Q_n^{(1)} \\ T_n^L, & \text{where } Q_n^{(1)} \leq Q_n^{\text{ion}} \leq Q_n^{(2)} \\ \frac{Q_n^{\text{ion}} - L V_n}{C_n^{\text{ion}} V_n}, & \text{where } Q_n^{\text{ion}} > Q_n^{(2)}. \end{cases} \quad (2.13)$$

where L is the volumetric heat of fusion, C_n^{ion} is the specific heat of the ion subsystem of the n -th nanoparticle, $T_n^L = T^L(R_n)$ is the melting temperature, taking into account the size of the nanoparticle [74], $Q_n^{(1)}$ is heat corresponding to the beginning of melting particles:

$$Q_n^{(1)} = C_n^{\text{ion}} V_n T_n^L, \quad (2.14)$$

and $Q_n^{(2)}$ corresponds to the heat at the end of the melting of the particle:

$$Q_n^{(2)} = Q_n^{(1)} + L V_n. \quad (2.15)$$

Thus, it becomes possible to determine the mass fraction f_n of the liquid phase from eq. (2.4):

$$f_n = \begin{cases} 0, & \text{where } Q_n^{\text{ion}} < Q_n^{(1)} \\ \frac{Q_n^{\text{ion}} - Q_n^{(1)}}{C_n^{\text{ion}} V_n}, & \text{where } Q_n^{(1)} \leq Q_n^{\text{ion}} \leq Q_n^{(2)} \\ 1, & \text{where } Q_n^{\text{ion}} > Q_n^{(2)} \end{cases} \quad (2.16)$$

The heat transfer rate between the particle and the environment can be determined from the following expression [75]:

$$v_n = -\varkappa \int_{S_n} \nabla T(\mathbf{r}, t) \cdot \mathbf{n} dS, \quad (2.17)$$

where \varkappa and $T(\mathbf{r}, t)$ are the thermal conductivity coefficient and ambient temperature, respectively, \mathbf{n} is the vector perpendicular to the surface of the NP. Integration of the expression is performed over the entire surface S_n of the NP. The heat transfer rate due to radiation is many times lower than the heat transfer rate due to heat conduction, therefore, in this model, the contribution of the former can be neglected.

Further, from the heat equation for the environment, we can determine the values $T(\mathbf{r}, t)$:

$$\frac{\partial T(\mathbf{r}, t)}{\partial t} = a_{\text{diff}} \Delta T(\mathbf{r}, t), \quad (2.18)$$

where a_{diff} is a diffusion coefficient of the environment. We use the following boundary conditions to solve these equations:

- particle and ambient temperatures were taken equal at the initial time $t = 0$: $T_n^{\text{ion}} = T_n^{\text{el}} = T(\mathbf{r}, t = 0) = T_0 = 300 \text{ K}$;
- ambient temperature on the surface of the substrate does not depend on time: $T(\mathbf{r}_{\text{sub}}, t) = T_0 = 300 \text{ K}$;
- ambient temperature is constantly at a distance infinitely remote from the system ($|\mathbf{r}| \gg \max_n(R_n)$): $T(x = \pm\infty, y, z, t) = T(x, y = +\infty, z, t) = T(x, y, z = \pm\infty, t) = 300 \text{ K}$;
- the ambient temperature on the surface of the particles is equivalent to the temperature of the ionic subsystem of the NP: $T(|\mathbf{r} - \mathbf{r}_n| = R_n, t) = T_n^{\text{ion}}$.

2.1.4 Thermodynamic properties of optical plasmonic waveguides

In this section I apply thermodynamic model for OPW. In general case, OPW is a chain of NPs with center-to-center distance bigger than diameter of NP. In most experimental setups the OPW is located on the substrate. The excitation of the OPW can be implemented in practice, for example, using a probe near-field optical microscope. The external field $\mathbf{E}_n = \mathbf{E}(\mathbf{r}_n)$ incident on the n -th NP located at the point \mathbf{r}_n can be described as:

$$\mathbf{E}_n = \mathbf{E}_0 \exp(i\mathbf{k}\mathbf{r}_n). \quad (2.19)$$

Often only first ($n = 1$) nanoparticle of the waveguide is considered to be excited by the external radiation [76–80], as a result of which $\mathbf{E}_n = 0$ for $n \neq 1$. In this case, the dipole moment \mathbf{d}_n induced on the n -th nanoparticle can be found by solving the equations of coupled dipoles (2.1), which will take the following form when taking into account the influence from the substrate and the interaction between all the particles:

$$\mathbf{d}_n = \varepsilon_h \alpha_n^e \left[\mathbf{E}_n \delta_{n1} + \sum_{m=1}^N \hat{\mathbf{G}}(\omega; \mathbf{r}_n, \mathbf{r}_m) \mathbf{d}_m \right], \quad (2.20)$$

δ_{n1} is the Kronecker symbol, $\hat{\mathbf{G}}(\omega; \mathbf{r}_n, \mathbf{r}_m)$ is a 3×3 the interparticle interaction tensor (Green's tensor) which describes the electromagnetic field at the point \mathbf{r}_n induced by an electric dipole located at the point \mathbf{r}_m and oscillating with a frequency of ω . In the general case, the Green's tensor has the following form:

$$\hat{\mathbf{G}}(\omega; \mathbf{r}_n, \mathbf{r}_m) = \hat{\mathbf{G}}_{\text{free}}(\omega; \mathbf{r}_n, \mathbf{r}_m) + \hat{\mathbf{G}}_{\text{refl}}(\omega; \mathbf{r}_n, \mathbf{r}_m), \quad (2.21)$$

where $\hat{\mathbf{G}}_{\text{free}}(\omega; \mathbf{r}_n, \mathbf{r}_m)$ and $\hat{\mathbf{G}}_{\text{refl}}(\omega; \mathbf{r}_n, \mathbf{r}_m)$ are Green's tensors describing the electric field in a homogeneous medium and the electric field reflected from the substrate, respectively. Expressions for $\hat{\mathbf{G}}_{\text{free}}(\omega; \mathbf{r}_n, \mathbf{r}_m)$ and $\hat{\mathbf{G}}_{\text{refl}}(\omega; \mathbf{r}_n, \mathbf{r}_m)$ are shown explicitly in the articles [81–83]. It should be noted that the summation in the expression (2.20) is performed over all indices. However, $\hat{\mathbf{G}}_{\text{free}}(\omega; \mathbf{r}_n, \mathbf{r}_n) = 0$, which means that each NP does not interact with itself.

2.1.5 Transmission and dispersion properties of optical plasmonic waveguides

Dispersion relations are one of the most important concepts that quantitatively determine the ability of a linear chain of plasmonic nanoparticles to support SPPs. There are various approaches to estimate dispersion relations of finite [84–87] and infinite [88–95] chains of NPs. In my thesis I use the eigendecomposition method of Ref. [96].

In the general case, according to the Bloch theorem, the dipole moment and the incident field can be described as $\mathbf{d}_n = \mathbf{d} \cdot \exp(iqn h)$ and $\mathbf{E}_n^{\text{ext}} = \mathbf{E}^{\text{ext}} \cdot \exp(iqn h)$, where q is the Bloch eigenvector. So, it is possible to rewrite (2.20) for a infinite chain of particles:

$$\left[\frac{1}{\alpha} \hat{I} - \sum_{n=-\infty}^{\infty} \hat{G}_{nm} e^{iqnh} \right] \mathbf{d} = \mathbf{E}^{\text{ext}}. \quad (2.22)$$

One can note that the expression in square brackets has the same dimension as the inverse dipole polarizability of the NP. Thus, according to the method of eigenvector decomposition, it is convenient to characterize the electromagnetic response of the OPW with the so-called *effective polarizability* $\tilde{\alpha}$ [96] such that $1/\tilde{\alpha}$ is an eigenvalue of the following equation:

$$\left[\frac{1}{\alpha} \hat{I} - \sum_{n=-\infty}^{\infty} \hat{G}_{nm} e^{iqnh} \right]. \quad (2.23)$$

The maxima of $\text{Im}[\tilde{\alpha}] = F(\omega, q)$ correspond to the resonances of the OPW, which represent the passband of the OPW, or, in other words, its dispersion relation. A significant advantage

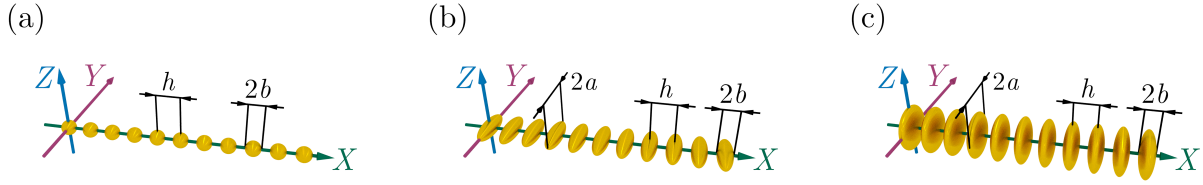


Figure 2.1: Schematic representation of the OPW from NPs of spherical shape (a), prolate spheroids (b) and oblate spheroids (c). Here we consider an OPW located along the X axis with a center-to-center distance h . The radius of the spherical particles is b as well as for the minor semiaxis for spheroids, while for the major semiaxis it is a . Image taken from Paper II. Copyright 2017 Elsevier.

of the eigenvector expansion method is the possibility to simultaneously estimate the eigenmodes of the OPW and their Q -factor [96, 97]. Thus, the function $\text{Im}[\tilde{\alpha}] = F(\omega, q)$ provides a complete physical representation of the dispersion relations for the OPW, which, generally speaking, is impossible to obtain using other methods considered in literature [84, 86, 88–90].

The calculation of the transmission spectrum of OPW is the most effective way to obtain actual damping of the SPP at the end of the waveguide. Suppose that the external field \mathbf{E}^{ext} excites only the first nanoparticle in the OPW in the form of a linear chain of N identical NPs fig. 2.1. The solution of eq. (2.20) on the right side provides the dipole moments \mathbf{d}_n induced on each nanoparticle in the OPW. Experimentally, the electric field strength at the end of the OPW is $I_N \propto \|\mathbf{d}_N\|^2$ which characterizes the SPP attenuation. Therefore, the SPPs propagation efficiency can be described by the following quantity [79]:

$$Q_{tr} = \frac{\|\mathbf{d}_N\|^2}{\|\mathbf{d}_1\|^2}. \quad (2.24)$$

Thus, one can refer the spectral dependence of Q_{tr} as the transmission spectrum of the OPW.

Three different shapes of NPs are considered in my thesis: spheres, oblate and prolate spheroids. The quasistatic polarizability eq. (2.3) of NPs with such shapes is determined by the following expression:

$$\alpha_n^{(0)} = \frac{V}{4\pi} \frac{\varepsilon - \varepsilon_h}{\varepsilon_h + D_{\text{stat}}(\varepsilon - \varepsilon_h)}, \quad (2.25)$$

where V is the volume of the NP, D_{stat} is the static depolarization coefficient [62].

For NPs with dimensions much smaller than the wavelength of the incident light, retarda-

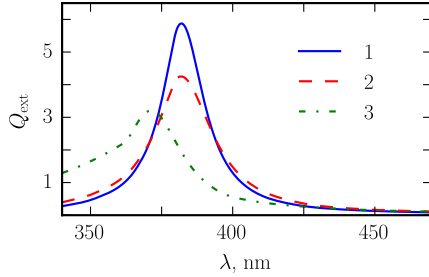


Figure 2.2: Extinction spectra of a single Ag NP with radius $R = 8$ nm for various values of temperature: 1 – room temperature; 2 – melting point, solid state; 3 – melting point, liquid state. Image taken from my article [100]. Copyright 2017 Elsevier.

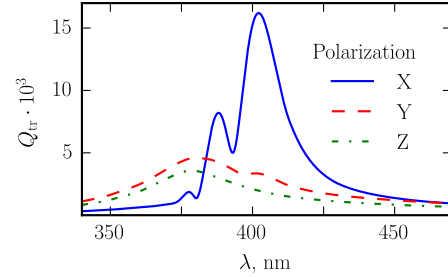


Figure 2.3: Transmission spectra of OPW for various polarizations of exciting laser radiation (see legend) at the initial moment of time $t = 0$ and room temperature $T = 300$ K. Image taken from my article [100]. Copyright 2017 Elsevier.

tion effects should be taken into account [60, 98]. Therefore, to adequately describe the electromagnetic properties, it is necessary to introduce the so-called dynamic correction [99] of the polarizability of spheroidal NPs. The polarizability α_n of the n -th NP in the OPW then takes the form:

$$\alpha_n = \alpha_n^{(0)} \left[1 - \frac{k^2}{l_E} D_{\text{dyn}} \alpha_0 - i \frac{2k^3}{3} \alpha_0 \right]^{-1}, \quad (2.26)$$

where $\alpha_n^{(0)}$ is defined by eq. (2.25), D_{dyn} is the dynamic geometric factor [99], l_E is the length of the NP semiaxis along which the electric field is directed. The static D_{stat} and dynamic D_{dyn} depolarization factors for oblate and prolate spheroids can be found using well-known expressions [62, 99]. For spherical NPs: $D_{\text{stat}} = 1/3$ and $D_{\text{dyn}} = 1$.

2.2 Results

2.2.1 Thermal and optical properties of optical plasmonic waveguides from silver nanoparticles

In my thesis I consider single Ag NPs in water and its extinction efficiency Q_{ext} as shown in eq. (2.27). Extinction efficiency is determined by extinction cross section σ_{ext} , which is a

sum of the cross sections due to absorption and scattering.

$$\begin{aligned} Q_{\text{ext}} &= \frac{\sigma_{\text{ext}}}{\pi R^2}, \\ \sigma_{\text{ext}} &= \frac{4\pi|\mathbf{k}|}{|\mathbf{E}_0|^2} \text{Im}(\mathbf{d} \cdot \mathbf{E}(\mathbf{r})). \end{aligned} \quad (2.27)$$

From fig. 2.2 it can be seen that the extinction efficiency of single spherical Ag NP with radius $R = 8$ nm decreases by 1.5 times for various temperatures and state of aggregation when the temperature of NP reaches the melting temperature ($T \approx 1080$ K for Ag). In addition, the maximum of the extinction spectrum is strongly shifted to the short-wavelength region at the end of melting, when the nanoparticle completely passes into the liquid state. In this case, the value of Q_{ext} decreases by half compared with a solid nanoparticle at room temperature. Thus, it becomes obvious that temperature effects will significantly affect the transmission properties of OPWs, especially if only the $n = 1$ nanoparticle is excited by the external radiation.

Figure 2.3 represents the frequency-dependent transmission (eq. (2.24)) for three different polarizations of the external field, which coincide with the Cartesian coordinate axes, at the initial moment of time $t = 0$, when temperature is equal to room temperature ($T = 300$ K) for the OPW from $N = 11$ Ag particles with the geometry described in fig. 2.1(a). The maximum value of Q_{tr} is reached at a wavelength of $\lambda = 402$ nm with the polarization directed along the X axis (see fig. 2.1(a)). Thus, only X polarization is of interest for the cases studied in my thesis, while for other polarizations I do not see any promising applications.

Next, I turn to the discussion of temperature kinetics in OPWs. Obviously, thermal effects directly depend on the intensity of the exciting laser radiation. For small values of intensity of the laser pulse, none of the nanoparticles reach the melting temperature. However, in this case it will be practically impossible to register an optical signal at the end of the chain due to the strong attenuation of the SPP. As can be seen from fig. 2.3 the amplitude of the SPP at the end of the waveguide decreases very much (here by 70 times), even in the case of the best transmission. For high values of intensity of the laser pulse, substantial heating of the nanoparticles will be observed. In this case, their resonance properties will be almost completely suppressed. Thus, I consider exciting laser radiation with an intermediate intensity located between these two cases. The results of numerical simulations show that for the intensity of a laser pulse being $I = 1.57 \times 10^8$ W/cm², only the first nanoparticle reaches the melting temperature. In this case, the transmission properties of the OPW will not decrease significantly. This value of the laser pulse intensity is standard for many lasers.

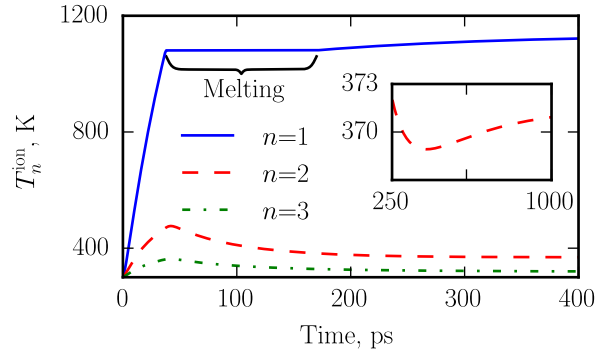


Figure 2.4: The temperature of the ionic subsystem T_n^{ion} of the first, second, and third particles in an OPW (with geometry from fig. 2.1(a)) after $t = 1$ ns excitation of a laser pulse with $\lambda = 402$ nm and $I = 1.57 \times 10^8$ W/cm² intensity. The inset shows the temperature T_2^{ion} in the time interval from $t = 250$ ps to $t = 1000$ ps. Image taken from my article [100]. Copyright 2017 Elsevier.

Figure 2.4 shows the time dependence of the temperature of the ionic subsystem for the first three NPs in an OPW, when the first nanoparticle is excited by a laser pulse at a wavelength of $\lambda = 402$ nm. It can be seen that the $n = 1$ nanoparticle reaches the melting temperature at $t = 37$ ps. Moreover, the maximum temperature reached by $n = 2$ and $n = 3$ nanoparticles at the same time: $T_2^{\text{ion}} \approx 480$ K and $T_3^{\text{ion}} \approx 350$ K, respectively. After $t = 37$ ps, the melting process of the $n = 1$ nanoparticle continues for about 134 ps and then its temperature increases slightly. After $t = 200$ ps, the temperature of the first three nanoparticles becomes constant: $T_1^{\text{ion}} \approx 1140$ K, $T_2^{\text{ion}} \approx 375$ K and $T_3^{\text{ion}} \approx 310$ K. However, the heat from $n = 1$ nanoparticles reaches $n = 2$ nanoparticles at $t \approx 420$ ps moment in time and T_2^{ion} slightly increases during the second half of the pulse (see insert in fig. 2.4). From fig. 2.4 it can be seen that the temperature of the second nanoparticle increases slightly over an extended period of time. The temperature T_n^{ion} of the $n \geq 4$ NPs also remains unchanged for the chosen parameters of laser radiation.

Figure 2.5 shows the transmission spectra (eq. (2.24)) of the OPW from spherical NP for various stages of melting of $n = 1$ nanoparticle. The transmission spectra of the OPW slightly changes when the $n = 1$ nanoparticle reaches its melting temperature ($t = 37$ ps, $T \approx 1080$ K - dashed red line). Changes in the transmission spectra are induced by changes in the dielectric constant of the particle. It should be noted that the NP is still in the solid state at $t = 37$ ps. However, a substantial suppression of the resonance properties of the $n = 1$ nanoparticle occurs at $t = 171$ ps, when it becomes completely liquid (right after the end of melting process). It is seen that the efficiency of the transmission of OPW decreases three times in this case (dash-dotted green line). As a result, the transmitted energy also

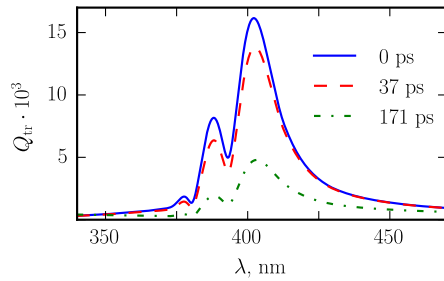


Figure 2.5: Transmission spectra of an OPW (with geometry from fig. 2.1(a)) excited by laser radiation with an intensity of $I = 1.57 \times 10^8 \text{ W/cm}^2$ at different points in time: initial time point $t = 0$ (solid line); start of melting of $n = 1$ nanoparticle, $t = 37 \text{ ps}$ (dashed line); end of melting of $n = 1$ nanoparticle, $t = 171 \text{ ps}$ (dash-dotted line). Image taken from Paper I. Copyright 2017 Optical Society of America.

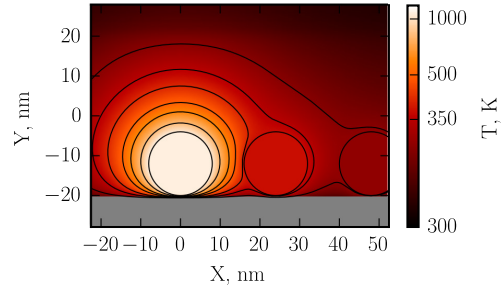


Figure 2.6: The temperature distribution T at time $t = 1 \text{ ns}$ for the first three nanoparticles (plane XOY , $z = 0$) in the OPW (with geometry from fig. 2.1(a)). The first nanoparticle is excited by a laser pulse with intensity $I = 1.57 \times 10^8 \text{ W/cm}^2$. We draw the attention of readers that the color scale is presented in a non-linear scale for clarity. Image taken from Paper I. Copyright 2017 Optical Society of America.

decreases. In turn, this leads to a decrease in the temperature of the second and subsequent particles (see fig. 2.4). A further increase in the temperature of the nanoparticles in the chain occurs due to heat exchange between them (see the inset in fig. 2.4).

I plot the temperature distribution in the XOY plane (at $Z = 0$) for the OPW at $t = 576$ ps on fig. 2.6. The technological substrate is depicted schematically (grey color). Clearly, the temperature substantially increases for only the first three NPs. Despite the fact that the temperature of the $n = 1$ NP reaches the melting point (according to fig. 2.4), heat transfer from more heated ones nanoparticles to less heated occurs through the interparticle environment.

2.2.2 Optical properties of optical plasmonic waveguides from titanium nitride nanoparticles

Refractory materials are often considered to be effective in avoiding the negative influence of thermal effects on the OPW functionality. It is important to mention that even though TiN does not melt, its permittivity is temperature-dependent, which is taken into account in my work. Therefore, in this section, I will consider the dispersion and transmission properties of OPWs from TiN nanoparticles. I assumed that the chain of nanoparticles is located in a homogeneous medium and only the first ($n = 1$) nanoparticle is excited. In this section, the discussion will be based on the fact that TiN NPs do not heat up to the melting temperature and do not reach a phase transition. So, I will move directly to the dispersion properties of OPW from TiN NPs.

Figures 2.7 and 2.8 represent values of $\log[\text{Im}(\tilde{\alpha})]$ from eq. (2.23) as a function of the frequency of SPP ω and eigenmodes of the wave vector q . According to the eigenvector expansion method, high values of $\text{Im}(\tilde{\alpha})$ correspond to high values of the Q eigenmode factor. While the summation in the eq. (2.23) occurs at infinity, we consider the OPW with a finite but sufficiently large number of particles, namely, $N = 1000$ NPs. I start with the OPW from spherical NPs whose dispersion relations are shown in the first column of figs. 2.7 and 2.8. It can be seen that SPPs efficiently propagate both for longitudinal (X) and transverse (Y) polarizations at frequencies $\omega \approx 2.5 - 3.5$ rad/fsec. However, the branch corresponding to the highest values of $\text{Im}(\tilde{\alpha})$ has a rather slight slope, which corresponds to a low group SPP velocity in this spectral range.

It was previously shown that the use of non-spherical NPs in OPWs significantly increases the group SPP velocity [86, 89] and at the same time minimizes the SPP suppression [101]. Thus, it is of interest to consider the dispersion relations in the OPW from prolate and oblate spheroids with different values of the semiaxes ratio b/a . From fig. 2.7 and 2.8 it

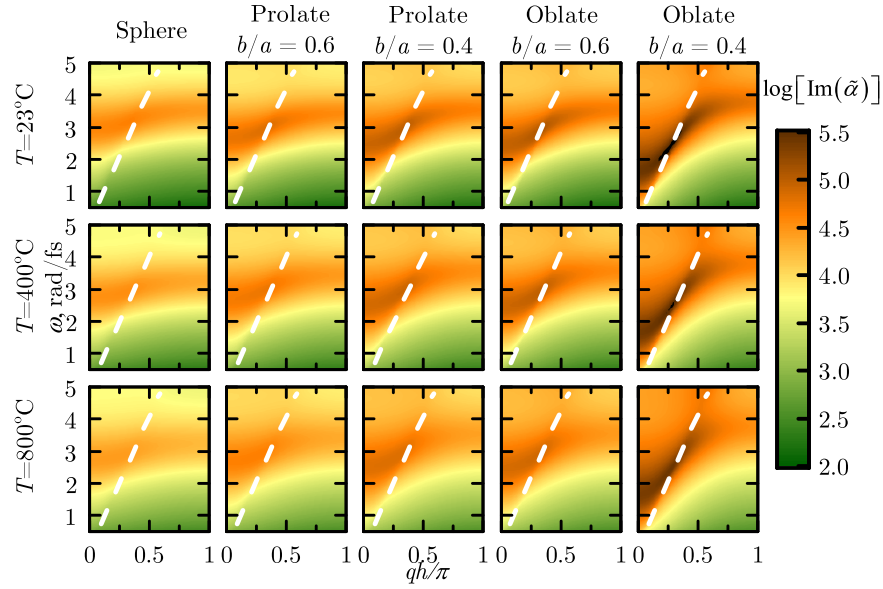


Figure 2.7: Dispersion relations for an OPW from spherical and spheroidal particles at various temperatures for the longitudinal (X) polarization of the SPP. White dashed line represents light line $\omega = q/c$. Image taken from Paper II. Copyright 2017 Elsevier.

can be seen that in the case of longitudinal polarization, the general shape of the dispersion curve is almost the same as for the OPW from spherical NPs. This behavior is explained by an insignificant difference in the depolarization coefficients L for different geometries of the NPs with the same values of the short semi-axis b parallel to the polarization of the SPP. However, for oblate spheroids with $b/a = 0.4$, the values of Q near the light line $\omega = q/c$ are significantly larger.

In the case of transverse polarization, the values of $\log[\text{Im}(\tilde{\alpha})]$ increase significantly, especially for the spectral range $\omega \approx 1.5\text{--}2.5$ rad/fsec for OPWs from prolate and oblate spheroids with $b/a = 0.4$. The dispersion dependencies for OPWs from oblate spheroids have an even greater slope compared to OPWs from prolate spheroids with the same values of b/a . In addition, the frequency of the eigenmodes decreases to $\omega \approx 1\text{--}2$ rad/fsec, which corresponds to the telecommunication wavelength range. In addition, the throughput of an OPW is increased in this case. Finally, the dispersion branch acquires a significant negative slope, which leads to an increase in the group velocity of the SPP and antiparallel propagation of the group and phase velocities of the SPP. The propagation of transversely polarized SPP with antiparallel group and phase velocities is described in detail in [89, 97, 102]. However, it should be noticed that the negative slope of the dispersion curve is not a direct evidence that OPWs are negative refractive metamaterials.

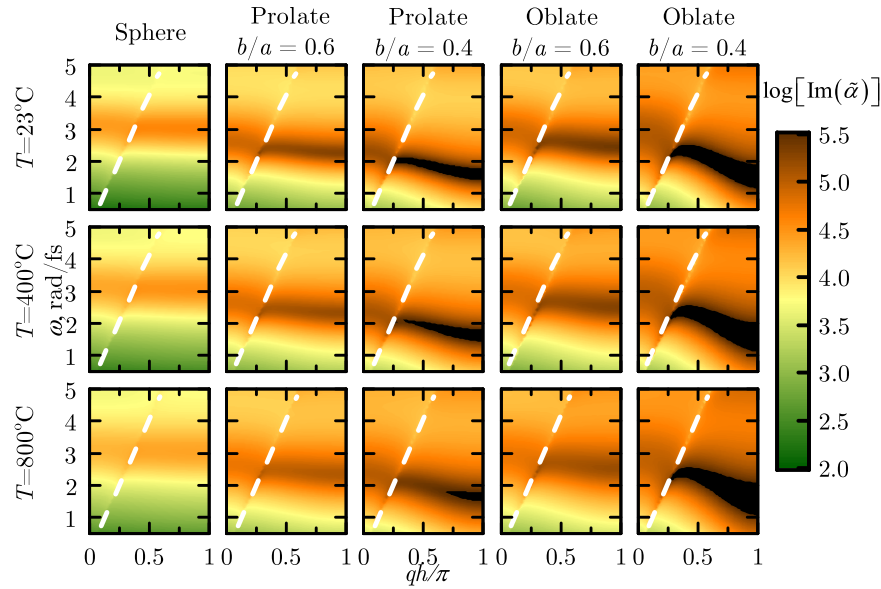


Figure 2.8: Dispersion relations for OPW from spherical and spheroidal particles at various temperatures for longitudinal (Y) polarization of the SPP. White dashed line denotes the light line $\omega = q/c$. Image taken from Paper II. Copyright 2017 Elsevier.

Despite the fact that TiN is thermally stable material [103], suppression of an SPP due to overheating of the OPW [100, 104] was describe in Section 2.1.3 is a crucial factor. From figs. 2.7 and 2.8 it can be seen that the dispersion relations of the OPW from TiN NPs remain almost unchanged even at $T = 800^\circ\text{C}$. The magnitude of the eigenmodes inevitably decreases at high temperature, but the suppression of the SPP is much lower than might be expected for ordinary plasmonic materials. Note that in my work the heating of the OPW is uniform, which is the most extreme case of overheating. In practice, only three neighboring NPs experience the highest heating in the case of local excitation of the SPP [100].

One of the interesting features that can be observed with a careful analysis of figs. 2.7 and 2.8 is that the SPP band (the spectral range corresponding to high- Q proper modes) varies significantly from longitudinal to transverse polarization for OPWs made from spheroids with $b/a = 0.4$. For longitudinal polarization, the frequency bandwidth of the OPW corresponds to the visible wavelength range, while for transverse polarization it lies in the telecommunication wavelength range. Thus, OPWs from prolate or oblate NPs can simultaneously operate in these two important wavelength ranges, which allows the use of such waveguides as hybrid photonic interconnectors.

Next, I turn to the transmission properties of OPW, considering the propagation of an SPP in short chains from $N = 20$ NPs. From fig. 2.9 it can be seen that the bandpass

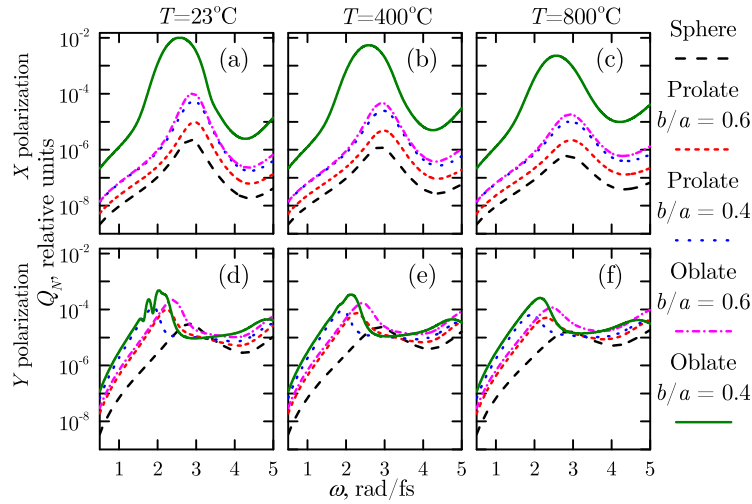


Figure 2.9: Transmission spectra of OPW from TiN NPs with various shapes for polarization X (a)-(c) and for polarization Y (d)-(f) SPP at various temperatures: (a), (d) $T = 23^\circ\text{C}$; (b), (e) $T = 400^\circ\text{C}$; (c), (f) $T = 800^\circ\text{C}$. Image taken from Paper II. Copyright 2017 Elsevier.

of the OPW can be adjusted by switching the polarization of the SPP from longitudinal to transverse. Moreover, Q_{tr} slightly decreases at high temperatures, which is crucial for waveguide applications of OPWs. As expected, the most effective SPP propagation occurs in OPWs from oblate spheroids with small aspect ratios (here $b/a = 0.4$), which is consistent with the results presented in [86, 101].

Finally, another attractive property of OPWs is their ability to confine electromagnetic energy at scales much shorter than the wavelength of the propagating excitation. This feature distinguishes OPWs from the classical [105] strip waveguides, whose transverse dimensions are usually comparable or several times larger than the wavelength of the propagating signal. Localization of the electromagnetic field near the OPW allows to locate several OPWs in close proximity to each other without the risk of an overlapping SPP propagating in a neighboring OPW, something which cannot be achieved in strip waveguides.

Figure 2.10 shows the temperature-dependent intensity distribution of $|\mathbf{E}|^2/|\mathbf{E}_0|^2$ for an OPW from TiN NPs at a distance 10 nm from the upper surface of the NPs. The frequencies ω were chosen to correspond to the maximum values of Q_{tr} for Y-polarization of the SPP from fig. 2.9 (d-f). It is shown that in the case of spherical NPs, the electric field is densely localized near the first excited NP and rapidly decays along the OPW. The most effective localization of the electric field is observed in the case of prolate spheroids. Distribution of $|\mathbf{E}|^2/|\mathbf{E}_0|^2$ looks completely different for OPWs from the oblate spheroids due to the high local field at the tips of oblate spheroids. Finally, due to the refractory behavior, the

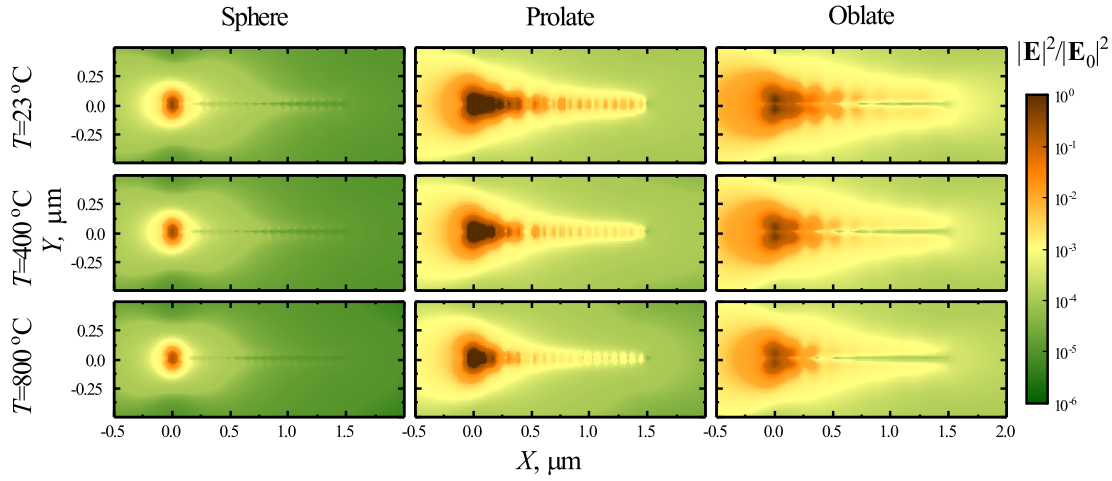


Figure 2.10: Localization of the electric field $|\mathbf{E}|^2/|\mathbf{E}_0|^2$ OPW from spherical, prolate and oblate nanoparticles (with $b/a = 0.4$ for both types of spheroids) TiN NPs for the Y polarization of SPP at different temperatures. The frequencies were taken in accordance with the maximum values of Q_{tr} from the fig. 2.9. In all cases, the first particle on the left is excited. Image taken from Paper II. Copyright 2017 Elsevier.

confinement of the electric field for OPWs from TiN NPs remains almost unchanged at high temperatures.

2.3 Conclusions for Chapter 2

In this chapter, an original theoretical model of my thesis was reviewed and summarized. It describes light-induced dipole interaction between nanoparticles and environment in high-intensity optical fields, taking into account thermal effects. The proposed model includes taking into account the temperature dependence of the dielectric constant of the particle material, as well as the heat exchange of nanoparticles with the environment. The model developed in this thesis was used to study the thermal effects that occur during the propagation of surface plasmon polaritons excited by pulsed laser radiation in an optical plasmonic waveguide (OPW). It was shown that thermal effects significantly decrease the efficiency of OPW transmission due to the suppression of the plasmon resonance of the nanoparticles. In this work, the optimal conditions for transmitting information with the optical waveguide were determined.

It was shown that TiN is a promising alternative material that can be used in OPWs in the form of chains of nanoparticles (NPs) that can support the effective propagation of

SPPs [106]. The bandwidth of linear periodic chains of titanium nitride (TiN) NPs can be adapted to both the visible range and the telecommunication wavelength range by changing the shape of the nanoparticles and polarization of the surface plasmon polariton (SPP). Despite the inevitable ohmic losses and overheating of nanoparticles, the SPP attenuation remains almost unchanged even at extremely high temperatures due to the pronounced refractory properties of TiN. Along with cheap methods of large-scale production of TiN nanoparticles, all these features make it a promising plasmonic material for waveguide applications using linear periodic chains of NPs.

The results obtained allow me to offer new applications of OPWs associated with their high sensitivity to the intensity of exciting radiation. Further development of the proposed model and the study of thermal effects in OPWs or other periodic nanostructures is promising and will open up new practical applications of plasmonic nanosystems [107].

Chapter 3

Collective effects in structures of resonant nanoparticles

Dielectric nanoparticles have attracted an increased interest in photonics due to their ability to preserve not only electric, but also magnetic dipole moments. In this chapter, based on the extended coupled dipole approximation, I review three types of defects in two-dimensional arrays of spherical Si nanoparticles that are studied in my thesis: disorder in the positions of Si nanospheres of the same size; size disorder of nanospheres located in an ordered two-dimensional lattice; and quasi-ordered two-dimensional arrays of nanospheres with the same size. A comprehensive analysis in my thesis of these scenarios reveals various effects of disorder on the coupling of electric dipole and magnetic dipole resonances with lattice modes. Next, I have demonstrated ED \leftrightarrow MD cross-interactions in sufficiently large NPs arrays, where such interactions are usually considered to be negligible.

3.1 Model

3.1.1 Extended coupled dipole approximation

Lets consider an array of N spherical NPs embedded in vacuum which is irradiated by electromagnetic plane waves with electric \mathbf{E}^0 and magnetic \mathbf{H}^0 components. The n -th particle located at \mathbf{r}_n acquires electric \mathbf{d}_n and magnetic \mathbf{m}_i dipole moments which are coupled to other dipoles and to an external electromagnetic filed via the extended coupled dipole equations [108–110]:

$$\mathbf{d}_n = \alpha^e \left(\mathbf{E}_{\text{inc}}(\mathbf{r}_n) + \sum_{j \neq n}^{N_{\text{tot}}} G_{nj} \mathbf{d}_j - \sum_{j \neq n}^{N_{\text{tot}}} \mathbf{g}_{nj} \times \mathbf{m}_j \right), \quad (3.1)$$

$$\mathbf{m}_n = \alpha^m \left(\mathbf{H}_{\text{inc}}(\mathbf{r}_n) + \sum_{j \neq n}^{N_{\text{tot}}} G_{nj} \mathbf{m}_j + \sum_{j \neq n}^{N_{\text{tot}}} \mathbf{g}_{nj} \times \mathbf{d}_j \right), \quad (3.2)$$

where α_n^e and α_n^m are electric and magnetic dipole polarizabilities [110] of the n -th particle, respectively, ε_0 and μ_0 are the dielectric constant and magnetic permeability of vacuum, $\mathbf{E}_n^0 = \mathbf{E}^0(\mathbf{r}_n)$, $\mathbf{H}_n^0 = \mathbf{H}^0(\mathbf{r}_n)$, and

$$\hat{G}_{nj} = A_{nj} \hat{I} + B_{nj} \left(\frac{\mathbf{r}_{nj} \otimes \mathbf{r}_{nj}}{r_{nj}^2} \right), \quad \hat{C}_{nj} = D_{nj} \frac{\mathbf{r}_{nj}}{r_{nj}} \times, \quad (3.3)$$

where \hat{I} is a 3×3 unit tensor, \otimes denotes a tensor product, and A_{nj} , B_{nj} and D_{nj} are defined as follows:

$$A_{nj} = \frac{\exp(ikr_{nj})}{r_{nj}} \left(k^2 - \frac{1}{r_{nj}^2} + \frac{ik}{r_{nj}} \right), \quad (3.4)$$

$$B_{nj} = \frac{\exp(ikr_{nj})}{r_{nj}} \left(-k^2 + \frac{3}{r_{nj}^2} - \frac{3ik}{r_{nj}} \right), \quad (3.5)$$

$$D_{nj} = \frac{\exp(ikr_{nj})}{r_{nj}} \left(k^2 + \frac{ik}{r_{nj}} \right), \quad (3.6)$$

Electric and magnetic dipole polarizabilities are explicitly defined as [62]:

$$\alpha_n^e = \frac{3i}{2k^3} \frac{m\psi_1(mkR_n)\psi_1'(kR_n) - \psi_1(kR_n)\psi_1'(mkR_n)}{m\psi_1(mkR_n)\xi_1'(kR_n) - \xi_1(kR_n)\psi_1'(mkR_n)}, \quad (3.7)$$

$$\alpha_n^m = \frac{3i}{2k^3} \frac{\psi_1(mkR_n)\psi_1'(kR_n) - m\psi_1(kR_n)\psi_1'(mkR_n)}{\psi_1(mkR_n)\xi_1'(kR_n) - m\xi_1(kR_n)\psi_1'(mkR_n)}, \quad (3.8)$$

where m is the refractive index of the NP material, R_n is the radius of the n -th particle, $\psi_1(x)$ and $\xi_1(x)$ are Riccati-Bessel functions, and prime denotes the derivation with respect to the argument in parentheses.

The essence of CLRs can be understood from a closed-form analytical solution of eq. (3.1) and eq. (3.2) obtained for an infinite array [3, 110]. In this case, $\mathbf{d}_n = \mathbf{d} \parallel \mathbf{E}_0$ and $\mathbf{m}_n =$

$\mathbf{m} \parallel \mathbf{H}_0$ for each NP [110], therefore, the last terms in eq. (3.1) and eq. (3.2) vanish, since $\mathbf{E}_0 \perp \mathbf{H}_0$. Thus, for a special case of a regular 2D lattice illuminated with a normally impinging wave with $|\mathbf{E}_0| = E_{0x}$ and $|\mathbf{H}_0| = H_{0y}$, the non-zero components of \mathbf{d} and \mathbf{m} are

$$d_x = \frac{E_{0x}}{1/\alpha^e - G_{xx}^0}, \quad m_y = \frac{H_{0y}}{1/\alpha^m - G_{yy}^0}, \quad (3.9)$$

where G_{xx}^0 and G_{yy}^0 are diagonal elements of the 3×3 tensor $G^0 = \sum_{j=2}^{\infty} G_{1j}$, and $(1/\alpha^{e,m} - G_{xx,yy}^0)^{-1}$ are effective electric and magnetic polarizabilities which capture the features of the NP's surrounding [110–112].

The electric \mathbf{d}_n and magnetic \mathbf{m}_n dipoles induced on each NP can be found from the solution of eq. (3.1). In this work, I describe the optical response of a finite array of NPs with the extinction efficiency:

$$Q_e = \frac{4k}{I_0 N R^2} \text{Im} \sum_{n=1}^N (\mathbf{d}_n \cdot \mathbf{E}_n^{0*} + \mathbf{m}_n \cdot \mathbf{H}_j^{0*}), \quad (3.10)$$

where I_0 is the intensity of the incident field, and the $*$ denotes a complex conjugate. In the general case of polydisperse array with $R_n \neq R$, the average radius $\langle R \rangle = \sum_{n=1}^N R_n / N$ is used to define Q_e . For an infinite array, after substituting eq. (3.9) in eq. (3.10), one gets:

$$Q_e^{\text{inf}} = \frac{4k}{R^2} \text{Im} \left[(1/\alpha^e - G_{xx}^0)^{-1} + (1/\alpha^m - G_{yy}^0)^{-1} \right]. \quad (3.11)$$

Though, higher-order multipoles in all-dielectric NPs are pronounced, for example, in large [113–115] and nonspherical [116] single Si NPs, or in structures of closely packed Si NPs [117], full-wave simulations and mode analysis [118] show that ED and MD are predominant in arrays of spherical Si NPs with $R = 65$ nm, and high order electric and magnetic field oscillations can be ignored in this case. Thus, the extended coupled dipole approximation accurately describes optical properties of arrays from relatively small Si NPs.

3.1.2 Types of imperfections in arrays on silicon nanoparticles

From eq. (3.1) and eq. (3.2) I can conclude that two types of disorder can be achieved [76]: off-diagonal and diagonal. These types affect either off-diagonal or diagonal elements of the interaction matrix in eq. (3.1) and eq. (3.2). The first type of disorder (off-diagonal) affects only tensors \hat{G}_{nj} and \hat{C}_{nj} which are the functions of the NPs positions, while the second type of disorder (diagonal) affects only $\alpha_n^{e,m}$ which are functions of the shape and size of the NPs.

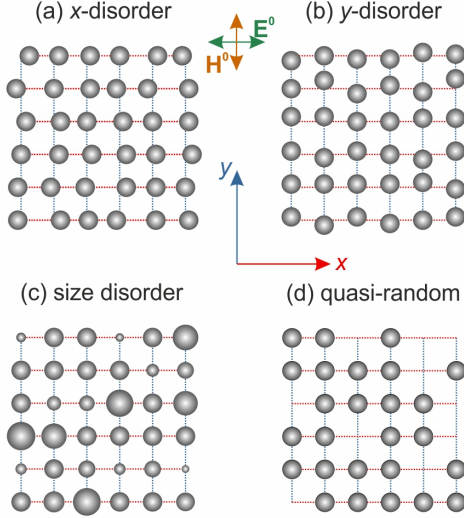


Figure 3.1: Schematic representation of different types of disorder considered in this work: (a) x -disorder, (b) y -disorder, (c) size disorder, and (d) quasi-random array. Image taken from Paper III. Copyright 2019 Optical Society of America.

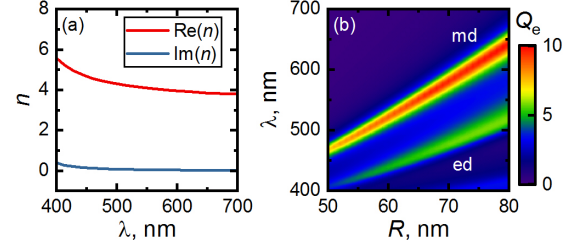


Figure 3.2: (a) Refractive index m of Si from Ref. [119]; (b) Extinction spectra for a single Si NP of various radii R taking into account high-order multipoles. Spectral positions of electric and magnetic dipole resonances are denoted as 'ed' and 'md', respectively. Image taken from Paper III. Copyright 2019 Optical Society of America.

For ordered arrays of NPs it is shown in fig. 3.3 that two types of couplings can be distinguished. For fixed wavelengths, the optical response of the lattices strongly depends on variations of either h_x and h_y . Thus, to get more insight, I introduce an off-diagonal disorder in the following manner. I study the positional disorder along the x axis keeping the y coordinates constant, and vice versa, as shown in fig. 3.1(a) and 3.1(b), respectively. I refer to these two types of positional disorders as x -disorder and y -disorder, correspondingly. For both cases, I introduce the deviation $\sigma_{x,y}$ which characterizes the degree of disorder. For each n -th particle with initial (x_n, y_n) coordinates, I randomly set new coordinates as (x_n^{dis}, y_n) for x -disorder and (x_n, y_n^{dis}) for y -disorder within the following limits:

$$x_n - \sigma_x \leq x_n^{\text{dis}} \leq x_n + \sigma_x, \quad \text{and} \quad y_n - \sigma_y \leq y_n^{\text{dis}} \leq y_n + \sigma_y. \quad (3.12)$$

Both x_n^{dis} and y_n^{dis} are randomly generated using a uniform distribution for each n -th NP and for each lattice with given (h_x, h_y) . Thus, the effects of positional disorder are uncorrelated.

The schematics of the lattice with diagonal (size) disorder is shown in fig. 3.1(c). In this specific case, I keep the original coordinates of each NP, and randomly change the radius R_n of each n -th NP within the following limits using a uniform distribution:

$$R_n - \sigma_R \leq R_n^{\text{dis}} \leq R_n + \sigma_R . \quad (3.13)$$

Again, as in the case of off-diagonal disorder, R_n^{dis} is introduced randomly for each NP and for each lattice configuration, which provides uncorrelated results. Finally, fig. 3.1(d) shows the last type of considered defects - a special combination of diagonal and off-diagonal disorders, which attract specific interest [120, 121]. It is a well-known fact that the coupling between a SPR of single NP and lattice modes strongly depends on the number of NPs in the array [112, 122]. Nevertheless, periodic lattices of strictly spaced NPs are usually considered studies of this effect of finite size. In this thesis, I fix the initial coordinates and NP sizes in the array and randomly remove the NP from the initial lattice, leaving the other NPs untouched. This type of imperfections is somewhat similar to vacancies in crystal structures. I refer to lattices shown in fig. 3.1(d) as quasi-random arrays. I emphasize that each lattice configuration for each type of disorder with given σ_x , σ_y and σ_R or number of NPs removed from the lattice in the case of quasi-random arrays reviewed here, has been simulated only once, without computing ensemble averages. The closeness to a statistical average has been guaranteed by simulating a reasonably large number of NPs.

3.2 Results

3.2.1 Periodic arrays of silicon nanoparticles

I start to shortly review the optical properties of a single Si nanosphere. Figure 3.2(a) shows the refractive index of Si used in my calculations [119], while fig. 3.2(b) shows the extinction efficiency Q_e for a single Si nanosphere of various radii R . For a single sphere, and only in this case, I calculate Q_e taking into account high-order harmonics [62] required for the convergence of the electromagnetic light scattering problem [123]. It can be seen from fig. 3.2(b) that indeed, for given sizes, the Si nanospheres have distinct and predominant ED and MD resonances in the visible wavelength range. This is a general reason to consider arrays from Si nanospheres with $R = 65$ nm radius. However, in the special case of a size disorder, all possible radii of NPs will fall into the range shown in fig. 3.2(b), i.e. $50 \text{ nm} \leq R_n \leq 80 \text{ nm}$. Therefore, the coupled dipole approximation can be used with strong confidence.

Next, it is insightful to discuss optical properties of *ordered* Si nanostructures. Figures 3.3(a) and 3.3(b) show two different types of lattices which have been studied in this thesis: with fixed period along the x axis, h_x , and varying period along the y axis, h_y , and with fixed h_y and varying h_x . Such variations of interparticle distances make it possible to get ED or

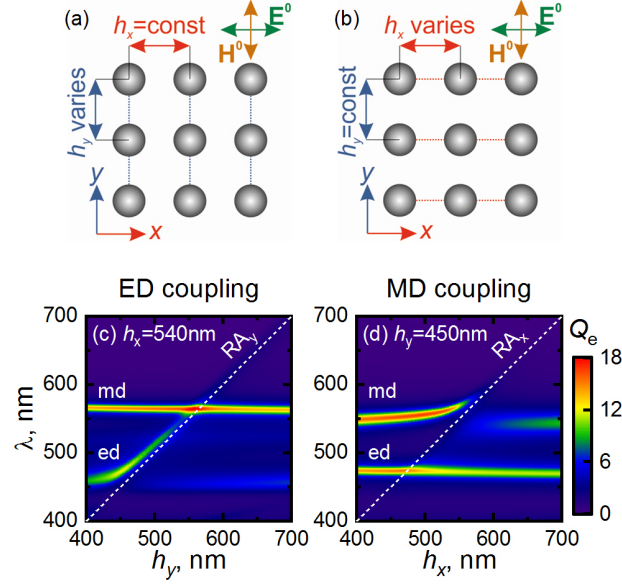


Figure 3.3: (a) and (b) Schematic representation, and (c) and (d) extinction spectra Q_e of ordered 2D lattices from $N = 20 \times 20$ Si NPs with $R = 65$ nm. Two configurations are considered: (left) fixed $h_x = 540$ nm and varying h_y , and (right) fixed $h_y = 450$ nm and varying h_x . Spectral positions of ED and MD resonances are denoted as 'ed' and 'md', respectively. Dashed RA_x and RA_y lines denote Rayleigh anomalies $\lambda = h_x$ and $\lambda = h_y$, correspondingly. Image taken from Paper III. Copyright 2019 Optical Society of America.

MD coupling with lattice modes [124]. In both cases, the incident electric \mathbf{E}^0 and magnetic \mathbf{H}^0 fields are aligned along the x and y axes, correspondingly. Lattices from $N = 20 \times 20$ Si NPs have been considered here.

In the first case, as it is clearly seen from fig. 3.3(c), ED strongly couples to lattice modes which leads to the emergence of quite sharp collective lattice resonances. The position of the MD resonance slightly shifts to shorter wavelengths for large h_y . Note that Q_e for MD increases near the Rayleigh anomaly $\lambda = h_y$. In the second case, according to fig. 3.3(d), the same strong coupling with lattice modes occurs for MD, while the position of ED gradually shifts to shorter wavelengths and the corresponding Q_e decreases with increasing h_x . Thus, the coupling occurs for the incident field (electric or magnetic) perpendicular to the axis along which the interparticle distance changes. In other words, for the particular case considered, EDs (\mathbf{E}^0 is parallel to x axis) couple to RA_y , and vice versa, MDs (\mathbf{H}^0 is parallel to y axis) couple to RA_x .

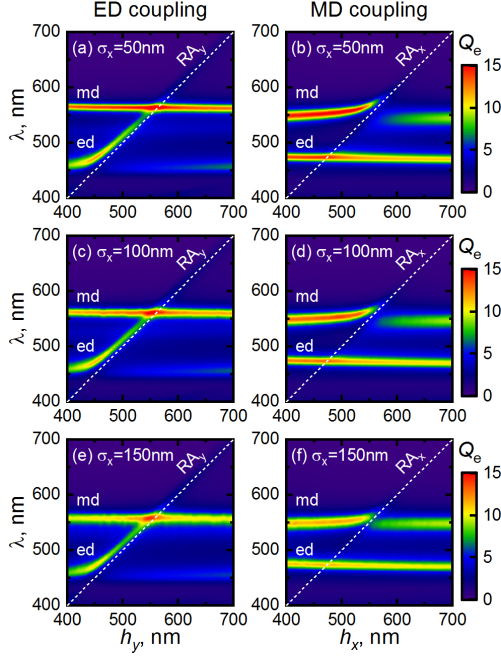


Figure 3.4: Extinction spectra Q_e for various degrees of positional disorder σ_x along the x axis, as shown in Fig 3.1(a). Image taken from Paper III. Copyright 2019 Optical Society of America.

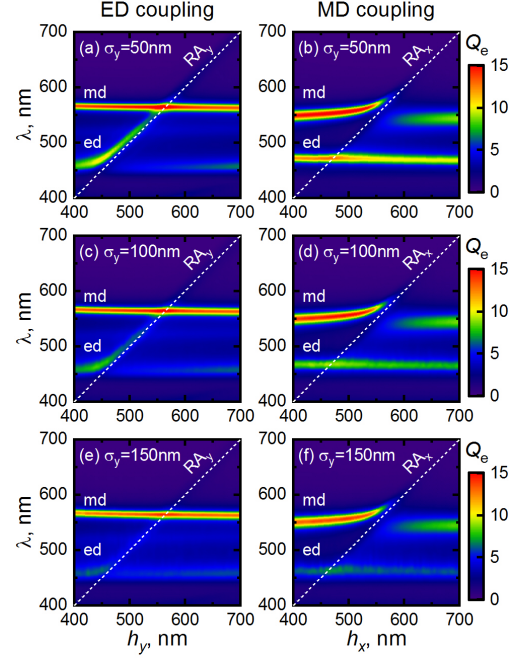


Figure 3.5: Extinction spectra Q_e for various degrees of positional disorder σ_y along the y axis, as shown in Fig 3.1(b). Image taken from Paper III. Copyright 2019 Optical Society of America.

3.2.2 Arrays of silicon nanoparticles with imperfections

Figures 3.4 and 3.5 show extinction spectra for arrays of NPs with different degrees of x - and y -disorders. It can be seen that these two types of positional disorders affect the optical properties of the NPs in a different way, depending on the coupling regime.

As it might be expected from the analysis of Fig. 3.3(d), the x -disorder significantly affects the MD, since the latter strongly couples to the Rayleigh anomaly RA_x . Clearly, from Fig. 3.4, one may observe slight suppression of the MD with the increasing of the degree of disorder, σ_x , both for ED and MD coupling scenarios. It can also be noticed that the coupling of MD and RA_x remains observable even for sufficiently large σ_x in Fig. 3.4(f), where MD is suppressed. ED remains almost the same for each case shown in Fig. 3.4.

Figure 3.5 shows an expected trend: since ED couples to RA_y , y -disorder affects only the former, keeping MD almost the same for various σ_y . However, Figs. 3.5(e)-3.5(f) show almost total suppression of ED for $\sigma_y = 150$ nm, while in the case of strong x -disorder shown in Figs. 3.4(e)-3.4(f), MD is quite pronounced. It might be explained by the fact that the

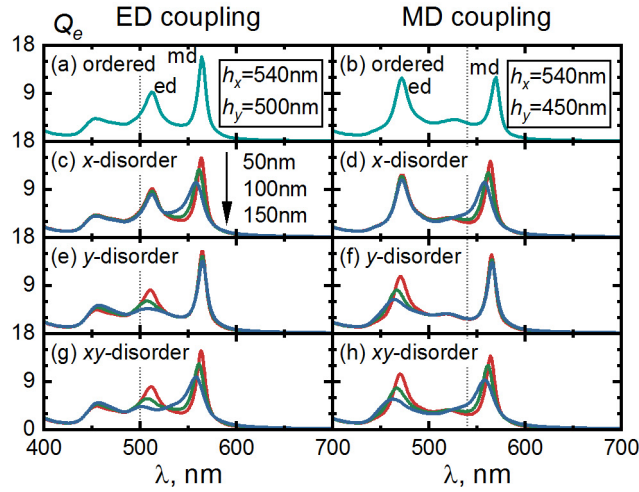


Figure 3.6: Extinction spectra Q_e of NPs arrays with ED coupling (left), and MD coupling (right) for various degrees of positional disorder σ_x (c,d), σ_y (e,f), and σ_{xy} (g,h). Corresponding values of h_x and h_y are shown in legends. Dashed vertical lines denote positions of Rayleigh anomalies RA_y at $\lambda = 500$ nm (left), and RA_x at $\lambda = 540$ nm (right). Image taken from Paper III. Copyright 2019 Optical Society of America.

MD response is stronger than the ED resonance in Si NPs of the considered sizes, according to Fig. 3.2(b). Thus, it is easier to suppress ED than MD for the same degree of positional disorders σ_y and σ_x , respectively.

Figure 3.6 shows the detailed comparison of the extinction spectra for arrays with ED or MD couplings. Indeed, x -disorder strongly suppresses the MD, while y -disorder suppresses the ED resonance. Since the ED is generally weaker than the MD, the former is almost completely disappears for high degrees of y -disorder. For the completeness, Figs. 3.6(g)-3.6(h) show the spectra for arrays with xy -disorder, which has been introduced in the same way as the x - and y -disorders, but with simultaneous randomization of both x_n and y_n coordinates of each NP. It can be seen that in the general case, such a combined disorder gives a superposition of both x - and y -disorders, which suppresses both ED and MD resonances.

Next, I move to the diagonal type of disordering. Figure 3.7 shows extinction spectra for arrays with various degrees of size disorder, σ_R . It is clearly seen that random variations of NP sizes strongly suppress both ED and MD resonances. However, MD remains observable only for $\sigma_R = 5$ nm, while for larger σ_R it almost completely disappears. Contrary, the ED resonance is preserved in all cases, and, of note, EDs strongly couple with Rayleigh anomalies, RA_y , even for high degrees of diagonal disorder, as shown in Fig. 3.7(e). This

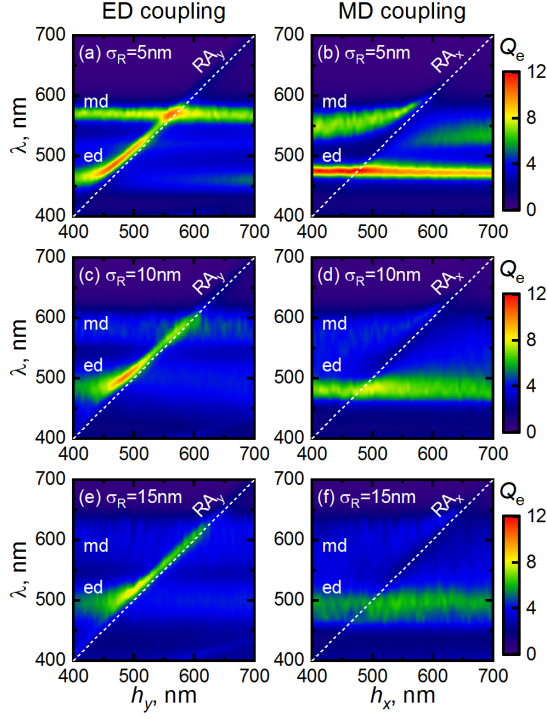


Figure 3.7: Extinction spectra Q_e for the same 2D lattices as in Figs. 3.3(c) and 3.3(d), but for various degrees of size disorder σ_R , as shown in Fig 3.1(c). Image taken from Paper III. Copyright 2019 Optical Society of America.

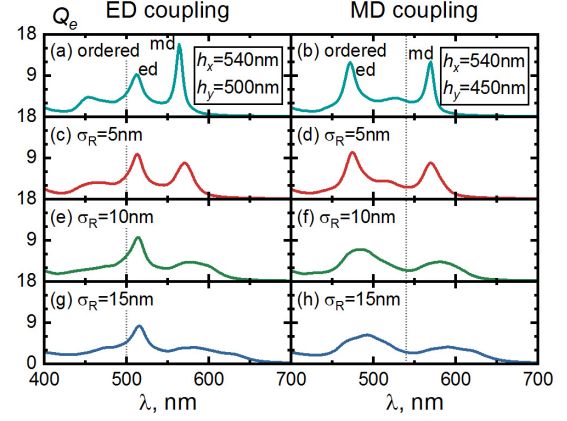


Figure 3.8: Extinction spectra Q_e of NPs arrays with ED coupling (left), and MD coupling (right) for various degrees of size disorder σ_R . Corresponding values of h_x and h_y are shown in legends. Dashed vertical lines denote positions of Rayleigh anomalies RA_y at $\lambda = 500$ nm (left), and RA_x at $\lambda = 540$ nm (right). Image taken from Paper III. Copyright 2019 Optical Society of America.

effect might be explained by the different behavior of polarizabilities α_i^e and α_i^m [110] which yields different impact of size disorder on ED and MD resonances.

To get a deeper insight, I plot Q_e for arrays with fixed h_x and h_y , as shown in Fig. 3.8. Indeed, Figs. 3.8(c), 3.8(e), 3.8(g) show that size disorder has a surprisingly weak effect on the ED resonance of arrays with strong ED coupling. It can be seen from Fig. 3.8(g) that the maximum Q_e for the ED resonance drops by no more than 10% for $\sigma_R = 15$ nm compared to the ordered array shown in Fig. 3.8(a). For arrays with MD coupling, Q_e for ED resonance drops stronger, by the factor of 2 for $\sigma_R = 15$ nm, as shown in Fig. 3.8(h). As for the MD resonance, in both the ED and MD coupling cases, the extinction efficiency for MD sharply drops for $\sigma_R = 5$ nm. For larger σ_R , the MD resonance becomes almost indistinguishable.

Based on the previous discussion of diagonal and off-diagonal types of disorders, I can

conclude that the simultaneous use of positional and dimensional disorders can lead to a superposition of effects as shown in Figs. 3.4, 3.5 and 3.7. Thus, I do not consider arrays of randomly located NPs of different size. Instead, I introduce a specific combination of positional and size disorders as shown in Fig. 3.1(d). These quasi-random arrays are fundamentally different from the ones shown in Figs. 3.1(a)-3.1(c) since random elements of the interaction matrix in (3.1) are strictly set to zero in the case of quasi-random arrays, while in the previously considered scenarios, off-diagonal or diagonal elements have acquired random deviations according to σ_x , σ_y or σ_R .

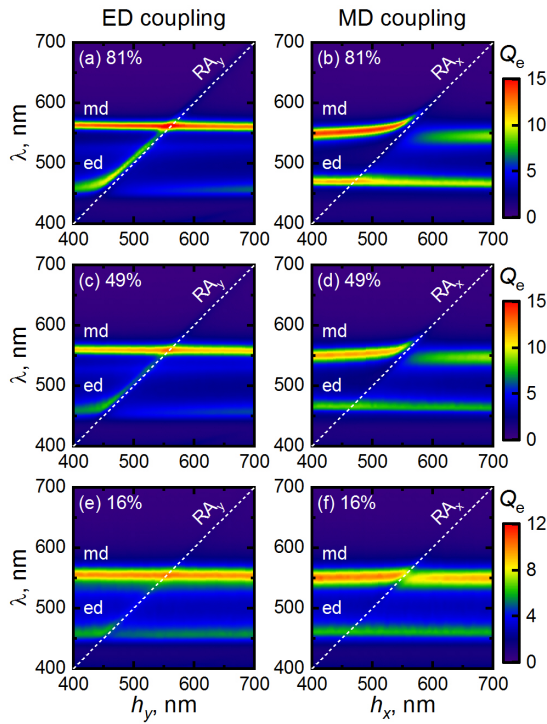


Figure 3.9: Extinction spectra Q_e for quasi-random 2D lattices, as shown in Fig 3.1(d), for different number of NPs: (a)-(b) 81% = 729, (c)-(d) 49% = 441, and (e)-(f) 16% = 144 kept untouched in $N = 30 \times 30$ arrays of NPs with $R = 65$ nm. Note the different color scale in the last row (e)-(f). Image taken from Paper III. Copyright 2019 Optical Society of America.

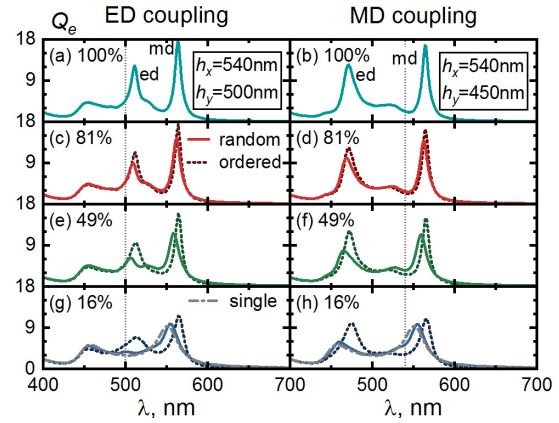


Figure 3.10: Extinction spectra Q_e of NPs arrays with ED coupling (left), and MD coupling (right) for (a)-(b) $N = 30 \times 30$ array, and for its various quasi-random modifications (solid lines): (c)-(d) 81% = 729, (e)-(f) 49% = 441, and (g)-(h) 16% = 144 NPs kept untouched. For comparison, Q_e of strictly periodic (dashed lines) arrays of the same number of NPs are shown: (c)-(d) $N = 27 \times 27 = 729$, (e)-(f) $N = 21 \times 21 = 441$, and (g)-(h) $N = 12 \times 12 = 144$, grey dash-dot lines show Q_e of a single Si NP with $R = 65$ nm. Image taken from Paper III. Copyright 2019 Optical Society of America.

Next, I review NPs with the same size, $R = 65$ nm, but increase their number to $N = 30 \times 30$ (while previously discussed arrays had $N = 20 \times 20$ NPs). Here, I randomly remove NPs,

leaving the rest (here 81%, 49% or 16%) of NPs untouched. I note that the consideration of larger arrays is preferable for this type of disorder, since coupling effects may be totally suppressed in arrays from a small number of NPs left in the lattice [112]. Nevertheless, in the smallest array considered here, I keep 144 quasi-randomly located NPs, which is sufficient for coupling effects to occur. Intuitively, one can expect suppression of the ED and MD resonances with an increase in the number of NPs removed from the ordered array. Indeed, Fig. 3.9 confirms such an expectation. However, it can be seen that lattices which contains 81% of the initial NPs have almost the same optical properties as the original periodic arrays. Moreover, Figs. 3.9(e)-3.9(f) show that ED and MD are coupled to Rayleigh anomalies (though quite weakly) in the arrays with only 16% NPs left, and extinction spectra of such arrays tend to become closer to the Q_e of a single NP.

For comparison, Fig. 3.10 shows spectra of ordered arrays (as in Figs. 3.3(a)-3.3(b)) from exactly the same number of NPs as in the quasi-random arrays, i.e. 27×27 , 21×21 , and 12×12 , and with the same h_x and h_y . It can be seen from Figs. 3.10(c)-3.10(d) that Q_e of the quasi-random array from 729 NPs is also almost the same as Q_e for the periodic 27×27 array. Moreover, even with the increasing number of NPs removed from the array, Q_e of the quasi-random lattices is quite close to strictly ordered arrays with the same number of NPs. However, in the most extreme cases of quasi-random arrays shown in Fig. 3.10(g)-3.10(h), the collective ED resonances are almost suppressed, while the MD coupling remains observable, though, the corresponding peak of the MD resonance is blue-shifted compared with the ordered arrays.

3.2.3 Finite size effects in arrays of silicon nanoparticles

From the analysis of (3.9), one could expect to observe resonances if $\text{Re}(1/\alpha^{e,m} - G_{xx,yy}^0)$ vanishes for either ED or MD resonances. Indeed, Fig. 3.11(a) shows that the dimensionless representation of the above parameter becomes zero near $\lambda \approx h_y$ and $\lambda \approx h_x$ for d_x and m_y , respectively, which corresponds to $(0, \pm 1)$ and $(\pm 1, 0)$ Wood-Rayleigh anomalies. Note that in the general case of $h_x \neq h_y$ considered here, a simple rotation of the incident field polarization, e.g. $(E_{0x}, 0, 0) \rightarrow (0, E_{0y}, 0)$, does not yield the interchange between ED and MD CLRs spectral positions, since it only implies the interchange $G_{xx}^0 \leftrightarrow G_{yy}^0$ in (3.9), which will likely violate the $\text{Re}(1/\alpha^{e,m} - G_{xx,yy}^0) = 0$ condition due to $G_{xx}^0 \neq G_{yy}^0$ and non-trivial wavelength dependence of polarizabilities $\alpha^{e,m}(\lambda)$ (Fig.(4) [110]).

Figure 3.11(b) shows that extinction spectra for finite-size arrays gradually approach the spectrum for the infinite lattice as N increases, which is consistent with reported trends for arrays of plasmonic NPs [112, 122]. Indeed, the ED CLR at $\lambda \approx 490$ nm for arrays with $N_{\text{tot}} > 50 \times 50$ becomes almost indistinguishable from one for the infinite array, as it

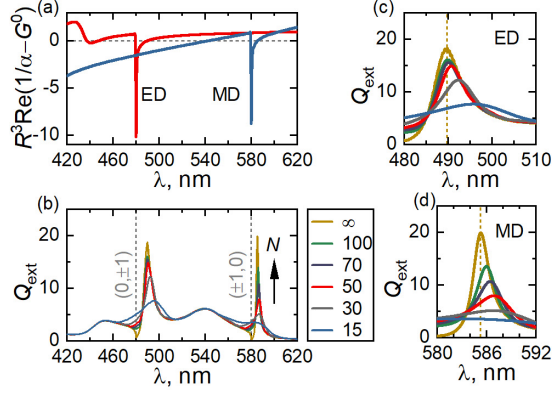


Figure 3.11: (a) Real parts of normalized denominators of (3.9) which correspond to d_x (ED) and m_y (MD); (b) Extinction efficiency for infinite (∞) and for $N \times N$ finite-size arrays; (c) and (d) zoomed-in spectra for ED and MD CLRs, respectively. Dashed vertical lines indicate the position of the CLR peak for the infinite array. Image taken from Paper VI. Copyright 2019 Optical Society of America.

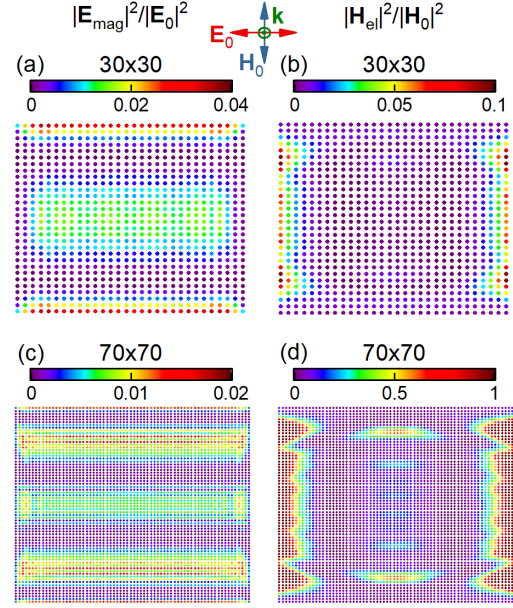


Figure 3.12: Normalized intensities of electric field induced by MDs (left) and of magnetic field induced by EDs (right) for $N \times N$ arrays at wavelengths: (a) 493 nm, (b) 588 nm, (c) 490 nm, (d) 586.5 nm. Each dot represents the NP, and the actual sizes of arrays vary for different $N \times N$. Image taken from Paper VI. Copyright 2019 Optical Society of America.

is clearly seen from Fig. 3.11(c). Of note, for plasmonic NPs arrays, the corresponding threshold, when Q_{ext} becomes almost the same for finite and infinite lattices is $\approx 20 \times 20$ NPs [112]. Analogously, Q_{ext} for an MD CLR at $\lambda \approx 586$ nm in finite-size arrays becomes similar to the infinite case if N grows, as it is shown in Fig. 3.11(d). However, what is really surprising and unexpected is that Q_{ext} of finite-size arrays is noticeably different even for the $N_{\text{tot}} = 100 \times 100$ case.

Figure 3.12 shows the corresponding intensities, i.e. $|\mathbf{E}_{\text{mag}}|^2$ and $|\mathbf{H}_{\text{el}}|^2$, for each NP in the array. It can be seen that the normalized intensity of the electric field induced by MDs is quite small compared to the incident field, and increases only at the boundaries of the array, which again agrees well with results for plasmonic NPs [122]. The maximum value of $|\mathbf{E}_{\text{mag}}|^2/|\mathbf{E}_0|^2$, which is already quite small for 30×30 arrays in Fig. 3.12(a), gradually decreases for larger arrays, and almost vanishes for the 70×70 array in Fig. 3.12(c), thus

providing negligible difference for ED CLR of infinite and sufficiently large finite-size arrays in Fig. 3.11(c). On the contrary, the maximum intensity of the magnetic field induced by electric dipoles, i.e. $|\mathbf{H}_{\text{el}}|^2/|\mathbf{H}_0|^2$, increases for larger arrays, and again a divergence takes place near the boundaries of the array. Although the overall contribution of the cross-interaction between EDs and MDs to $Q_{\text{ext}}^{\text{fin}}$ gradually decreases as N grows, the “boundary effect” is pronounced even for sufficiently large arrays, and thus can not be completely ignored in this case.

3.2.4 Optical filters based on arrays of plasmonic nanoparticles

In the previous section I showed that geometric parameters of an array of NPs, such as the interparticle distance, size and shape of the nanoparticles, significantly affect the position of electric and magnetic dipole resonances and may lead to suppression of the MD resonance, as well as the ED resonances. However, with proper parameters of the array it is also possible to prevent the appearance of several close lines in the spectrum instead of one line, which might be important for selective narrow-band filters in the tunable spectral range. To illustrate this I consider 2D arrays of nanodisks with height H and radius R arranged in a regular square lattice with period h . The arrays are embedded in a homogeneous environment with refractive index $n_m = 1.45$, which corresponds to quartz in the spectral range under study. Such structures can be fabricated using a lithography technique on a quartz substrate and subsequent sputtering a layer of quartz on top of the array. A homogeneous environment is an important factor in the model, because the Q-factor of the CLR drops dramatically in the case of a half-space geometry, where the substrate and the superstrate have different refractive indices [125]. The reflection spectra of such structures are calculated with a commercial FDTD method software. FDTD is a widely used computational method of electrodynamics, which in general shows excellent agreement with experimental results for CLR [11, 24, 126–128]. The optical response of the infinite array is simulated by considering a single particle unit cell with periodic boundary conditions applied at the lateral boundaries of the simulation box and perfectly matched layers used at the remaining top and bottom sides. Arrays are illuminated from the top by plane waves with normal incidence. The reflection has been calculated at the top of the simulation box using a discrete Fourier transform monitor which is placed above the plane-wave source. An adaptive mesh has been used to accurately reproduce the nanodisk shape. Finally, extensive convergence tests for each set of parameters have been performed to avoid undesired reflections on the perfectly matched layers.

The suppression of surface plasmon resonances under extreme conditions was studied in the papers [104, 129, 130] in my thesis. It was shown that heating of nanoparticles by pulsed

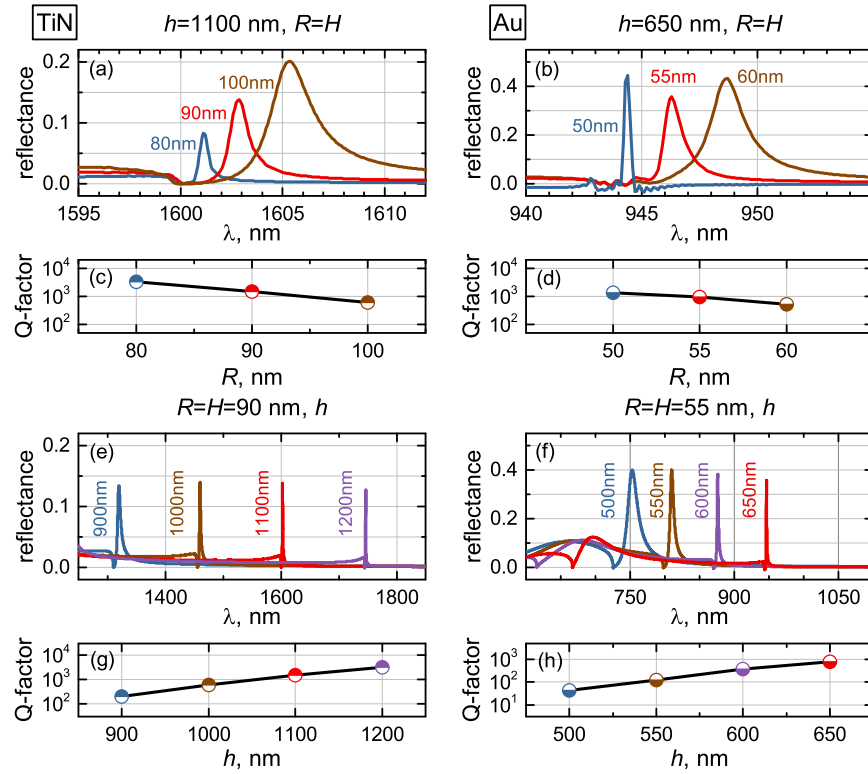


Figure 3.13: Reflection spectra for TiN (left) and Au (right) nanodisks arrays with: (a) fixed $h = 1100$ nm, and for different $R = H$ as shown in legend; (b) fixed $h = 650$ nm, and for different $R = H$ as shown in legend; (c) and (d) corresponding quality factors of CLRs; (e) fixed $R = H = 90$ nm and for different h as shown in legend; (f) fixed $R = H = 55$ nm and for different h as shown in legend; (g) and (h) corresponding quality factors of CLRs. Image taken from Paper IV. Copyright 2019 Optical Society of America.

laser radiation results in a reduction of the Q-factor and CLR amplitude. In particular, for the CLR at $\lambda = 1100$ nm in Fig 3.13, the Q-factor is $1.5 \cdot 10^3$ at $T = 23^\circ\text{C}$, $Q = 1.1 \cdot 10^3$ at $T = 400^\circ\text{C}$, and $Q = 0.7 \cdot 10^3$ at $T = 900^\circ\text{C}$. Thus, the high radiation resistance of TiN can be an additional advantage when using arrays exhibiting CLRs at high temperatures [131]. The use of TiN as a plasmonic material with high radiation resistance provides an extreme stability at high temperatures compared to conventional plasmonic materials (Au and Ag). Au nanodisks arrays (Fig. 3.13) demonstrate CLRs in the long-wavelength part of the visible and near IR ranges.

3.3 Conclusions for Chapter 3

The effect of various types of disordering on the optical response of $2D$ arrays of spherical Si nanoparticles was theoretically analyzed in my thesis. Electric and magnetic dipole resonances dominate in spherical Si nanoparticles (NPs) in the considered range of $50 \text{ nm} \leq R \leq 80 \text{ nm}$, so I used the extended coupled dipole approximation, which adequately describes the electromagnetic properties of arrays of Si NPs [118, 132].

First, I showed the existence of two types of collective resonances in $2D$ arrays arising from the strong coupling of electrical or magnetic dipole resonances of one NP with the lattice modes (Rayleigh anomalies) of the $2D$ array. Such a connection arises when the corresponding component of the incident field (electric or magnetic) is orthogonal to the variable period (h_y or h_x) of the lattice, and the other period (h_x or h_y) is constant [124]. Second, I showed that the electric and magnetic response is affected by positional disorder only when the low frequencies are displaced along an axis orthogonal to the corresponding component of the incident electromagnetic illumination. In my case, for $\mathbf{E}^0 \parallel x$ and $\mathbf{H}^0 \parallel y$, the electric and magnetic dipole resonances are strongly suppressed only for y or x disordering, respectively. Obviously, both resonances change when the nanoparticles are shifted along the x and y axes at the same time.

Next, I showed that the collective magnetic dipole response almost completely disappears in the case of diagonal (dimensional) disordering with $\sigma_R > 5 \text{ nm}$. However, the electric dipole moment remains quite stable, especially in the case of strong collective coupling between the electric dipole resonance and lattice modes, even for strongly polydisperse arrays with $\sigma_R = 15 \text{ nm}$. I considered quasi-random arrays as a special combination of diagonal and diagonal disorders. Instead of simultaneously displacing the nanoparticles and changing their sizes, I arbitrarily removed the nanoparticles from the lattice, leaving other nanoparticles at the starting points with the original sizes. It was noted that in the lattice where only 16% of the nanoparticles remained, collective electric and magnetic resonances

are observed. However, the extinction spectra of such arrays are, as a rule, similar to the spectra of a single nanoparticle. Furthermore, I have shown that the finite size of arrays of dielectric NPs plays an important role for the emergence of both electric dipole (ED) and magnetic dipole (MD) collective lattice resonances (CLR). While ED CLR in finite-size arrays converge to the infinite-array model for $\approx 50 \times 50$ NPs, MD CLR in finite-size arrays are quite different from the ones of infinite arrays even for 100×100 NPs, thus the common use of numerical and theoretical models for infinite arrays should be handled with great caution.

The reviewed results provide a comprehensive analysis and understanding of the effect that disordering has on collective resonances as well as effect of finite size in $2D$ arrays of dielectric nanoparticles. Although I examined the special case of spherical nanoparticles of Si embedded in vacuum, similar trends can be expected for dielectric arrays of other forms or materials, see [133], if higher-order multipoles can be neglected.

In this section I showed that the geometric parameters of arrays of dielectric nanoparticles, such as the period, size and shape of nanoparticles, significantly affect the position of the electric dipole resonance in the spectrum and can suppress the magnetic dipole resonance. A clever choice of geometric parameters can also prevent the appearance of several close lines or their splitting in the reflection spectrum instead of one line, which is unacceptable for selective narrow-band filters in the tunable spectral range. Arrays of nanoparticles in the reflection mode demonstrate the effect of optical filtering with fine tuning of the spectral position of the resonance line to the required wavelength by tilting the grating with respect to the incident radiation.

Chapter 4

Extended discrete interaction model for calculating optical properties of plasmonic nanoparticles

Finally, I present a new atomistic model for plasmonic excitations and optical properties of metallic nanoparticles (NPs). This model collectively describes the atomic complete response in terms of fluctuating dipoles and charges that depend on the local environment and on the morphology of NPs. This could be single element metal NPs as well as composite or alloy structure. Being atomic dependent, the model describes the total optical properties, the complex polarizability and the plasmonic excitation of a cluster and can refer these properties to a detailed level where geometric characteristics of the cluster plays a role, making it possible to explore the role of material, alloy mixing, size, form shape, aspect ratios, and other geometric factors, down to the atomic level. My conviction is that it will be useful for the design of plasmonic NPs with particular strength and field distributions, and can have wide ramifications in bioimaging, where small plasmonic particles often are desired. The model is parameterized from experimental data and is at present practically implementable for NPs up to more than 12 nm, for nanorods even more, thus covering a significant part of the gap between the scales where quantum calculations and classical models based on the bulk dielectric constant. I have applied the method to both spherical and cubical clusters along with nanorods and hollow NPs and have demonstrated the size and shape dependence of the plasmonic excitations and connected this to the geometry of the NPs using the plasmon length.

4.1 Model

4.1.1 Extended discrete interaction model

Similarly to the original DIM suggested by Jensen *et al.* [134, 135] the ex-DIM [136] aims to describe the polarizability and optical properties of metallic nanoparticles by representing the nanoparticle as a collection of interacting atomistic charges and dipoles. The starting point of both models is a Lagrangian with an energy expression for interacting fluctuating charges and dipoles in an external electric field subject to a charge equilibration constraint:

$$\begin{aligned}
 L[\{\boldsymbol{\mu}, q\}, \lambda] = & E[\{\boldsymbol{\mu}, q\}] - \lambda(q^{tot} - \sum_i^N q_i) \\
 = & \frac{1}{2} \sum_i^N q_i \mathbf{c}_{ii}^{-1} q_i + \frac{1}{2} \sum_i^N \sum_{j \neq i}^N q_i \mathbf{T}_{ij}^{(0)} q_j + \frac{1}{2} \sum_i^N \boldsymbol{\mu}_i \boldsymbol{\alpha}_{ii}^{-1} \boldsymbol{\mu}_i \\
 & - \frac{1}{2} \sum_i^N \sum_{j \neq i}^N \boldsymbol{\mu}_i \mathbf{T}_{ij}^{(2)} \boldsymbol{\mu}_j - \sum_i^N \sum_{j \neq i}^N \boldsymbol{\mu}_i \mathbf{T}_{ij}^{(1)} q_j + \sum_i^N q_i \mathbf{V}^{ext} \\
 & - \sum_i^N \boldsymbol{\mu}_i \mathbf{E}^{ext} - \lambda(q^{tot} - \sum_i^N q_i).
 \end{aligned} \tag{4.1}$$

In Eq. (4.1) the first term is the self-interaction energy of fluctuating charges, the second term is the interaction energy between fluctuating charges, the third term is the self-interaction energy of fluctuating dipoles, the fourth term is the interaction energy between fluctuating charges and dipoles, the fifth term is the interaction energy between fluctuating dipoles, the sixth term is the interaction energy between fluctuating charges and the external potential, the sixth term is the interaction energy between fluctuating dipoles and the external field, and the last term is a charge equilibration condition expressed via the Lagrangian multiplier λ . Here, the q_i is the fluctuating charge assigned to the i -th atom, $\boldsymbol{\mu}_i$ is the fluctuating dipole assigned to the i -th atom, the \mathbf{c}_{ii} is the i -th charge self-interaction tensor, the $\boldsymbol{\alpha}_{ii}$ is the i -th dipole self-interaction tensor, the $\mathbf{T}_{ij}^{(0)}$, $\mathbf{T}_{ij}^{(1)}$, and $\mathbf{T}_{ij}^{(2)}$ are the electrostatic interaction tensors, the \mathbf{V}^{ext} is the external potential, the \mathbf{E}^{ext} is the external electric field, q^{tot} is the total charge of the NP, and N is the total number of atoms in a NP. Similarly to DIM and cd-DIM, our ex-DIM uses Gaussian electrostatics to describe the interaction of fluctuating charges and dipoles. However, in our model normalized Gaussian charge distributions are explicitly dependent on the coordination number of the atom with which it is associated (see Eq. (4.10)), and thus the electrostatic interaction tensors, $\mathbf{T}_{ij}^{(0)}$, $\mathbf{T}_{ij}^{(1)}$, and $\mathbf{T}_{ij}^{(2)}$, have more complex form compared to the ones used in DIM or cd-DIM. Assuming we have two Gaussian charge distributions, $G(\mathbf{r}; f_{cn}, \mathbf{C})$ and $G(\mathbf{r}'; f'_{cn}, \mathbf{D})$ centred on the i -th and j -th

atoms with position vectors \mathbf{C} and \mathbf{D} , the electrostatic interaction tensor $\mathbf{T}_{ij}^{(0)}$ between these charges can be computed as

$$\mathbf{T}_{ij}^{(0)} = \int \int \frac{G(\mathbf{r}; f_{cn}, \mathbf{C})G(\mathbf{r}'; f'_{cn}, \mathbf{D})}{|\mathbf{r} - \mathbf{r}'|} d\mathbf{r}' d\mathbf{r} = \frac{erf(\gamma r_{ij})}{r_{ij}} \quad (4.2)$$

$$\gamma = \sqrt{\frac{a_{cn}a'_{cn}}{a_{cn} + a'_{cn}}} \text{ and } r_{ij} = |\mathbf{C} - \mathbf{D}|.$$

Following A. Mayer [137] the higher order electrostatic interaction tensors, $\mathbf{T}_{ij}^{(1)}$, and $\mathbf{T}_{ij}^{(2)}$, can be obtained by taking the derivatives of $\mathbf{T}_{ij}^{(0)}$ with respect to i -th atom coordinates i.e.

$$\mathbf{T}_{ij}^{(1)} = -\nabla_{\mathbf{r}_i} \mathbf{T}_{ij}^{(0)} = \frac{\mathbf{r}_{ij}}{r_{ij}^3} \left[erf(\gamma r_{ij}) - \frac{2\gamma r_{ij}}{\sqrt{\pi}} exp(-\gamma^2 r_{ij}^2) \right], \quad (4.3)$$

$$\begin{aligned} \mathbf{T}_{ij}^{(2)} &= -\nabla_{\mathbf{r}_i} \otimes \nabla_{\mathbf{r}_j} \mathbf{T}_{ij}^{(0)} = \frac{\mathbf{r}_{ij} \otimes \mathbf{r}_{ij} - r_{ij}^2 \mathbf{I}}{r_{ij}^5} \left[erf(\gamma r_{ij}) - \frac{2\gamma r_{ij}}{\sqrt{\pi}} exp(-\gamma^2 r_{ij}^2) \right] \\ &\quad - \frac{4\gamma^3 \mathbf{r}_{ij} \otimes \mathbf{r}_{ij}}{\sqrt{\pi} r_{ij}^2} exp(-\gamma^2 r_{ij}^2). \end{aligned} \quad (4.4)$$

Above given expressions for interaction tensors can be easily reduced to the ones used in DIM if one replaces coordination number dependent Gaussian exponents, a_{cn} and a'_{cn} , with appropriate effective radii (see Eqs. (11) – (13) in Jensens work [135]). The fluctuating charges and dipoles are determined by minimizing the energy $E[\{\boldsymbol{\mu}, q\}]$. According to Jensen *et al.* [135] this minimization problem can be recast into a problem of solving a set of linear equations:

$$\begin{pmatrix} \mathbf{A} & -\mathbf{M} & \mathbf{0} \\ -\mathbf{M}^T & -\mathbf{C} & \mathbf{1} \\ \mathbf{0} & \mathbf{1} & 0 \end{pmatrix} \begin{pmatrix} \boldsymbol{\mu} \\ \mathbf{q} \\ \lambda \end{pmatrix} = \begin{pmatrix} \mathbf{E}^{\text{ext}} \\ \mathbf{V}^{\text{ext}} \\ q^{\text{tot}} \end{pmatrix}, \quad (4.5)$$

where the column vector $\boldsymbol{\mu}$ is the collection of $\boldsymbol{\mu}_i$ dipoles, the column vector \mathbf{q} is the collection of q_i charges, λ is a Lagrangian multiplier associated with charge equilibration condition. The matrix elements of \mathbf{A} , \mathbf{C} , and \mathbf{M} matrices are defined as

$$\begin{aligned} \mathbf{A}_{ij} &= \delta_{ij} \boldsymbol{\alpha}_{ij}^{-1} - (1 - \delta_{ij}) \mathbf{T}_{ij}^{(2)}, \\ \mathbf{C}_{ij} &= \delta_{ij} \mathbf{c}_{ii}^{-1} + (1 - \delta_{ij}) \mathbf{T}_{ij}^{(0)}, \\ \mathbf{M}_{ij} &= (1 - \delta_{ij}) \mathbf{T}_{ij}^{(1)}. \end{aligned} \quad (4.6)$$

Equation (4.5) can be solved by inversion of the left-hand side matrix for small- and medium-size nanoparticles or by the iterative approach, like the conjugate gradient method for large size nanoparticles in an external field and potential. In the calculations presented here I solve the linear equations by inversion for each frequency since I do not apply an external field. After that the fluctuating charges and dipoles are determined the polarizability of the NP can be directly obtained by computing the second derivative of $E[\{\boldsymbol{\mu}, q\}]$ with respect to external field \mathbf{E}^{ext} . According to Jensen *et al.* [135, 138] the polarizability of a NP can be defined as

$$\boldsymbol{\alpha}^{np} = \sum_i^N \frac{\partial \boldsymbol{\mu}_i}{\partial \mathbf{E}^{\text{ext}}}. \quad (4.7)$$

The above described scheme for determination of the polarizability of a nanoparticle is generic and has been employed in the original, coordination dependent and extended discrete interaction models [134, 139–143]. The differences between these models originate from the functional form used to describe the fluctuating charges and dipoles and from the parameterization of the self-interaction and electrostatic interaction tensors. To lay the foundation for our extended discrete interaction model I first consider the parameterization of DIM and cd-DIM. In the original DIM model the self-interaction tensors (\mathbf{c}_{ii} and $\boldsymbol{\alpha}_{ii}$) are parameterized using atomistic capacitance and polarizability derived from bulk material properties, and the electrostatic interaction tensors ($\mathbf{T}_{ij}^{(0)}$, $\mathbf{T}_{ij}^{(1)}$, and $\mathbf{T}_{ij}^{(2)}$) are computed using normalized Gaussian charges and dipoles with parametrization using TDDFT. In the cd-DIM, the fluctuating charges are excluded from the energy expression $E[\{\boldsymbol{\mu}, q\}]$, the self-interaction tensor ($\boldsymbol{\alpha}_{ii}$) between dipoles is parameterized using a coordination number dependent atomistic polarizability derived via the Clausius-Mossotti relation [144], and the electrostatic interaction tensor ($\mathbf{T}_{ij}^{(2)}$) is computed the same way as in DIM. In order to extend these models and achieve a description of more complex surface topologies, I spatially spread in our model the Gaussian dipoles and charges in a way that they explicitly depend on their local chemical environment. Here, I use the scheme of Grimme [145], originally proposed for the computation of dispersion corrections in DFT calculations, for evaluating atomic coordination numbers. The atomic coordination number f_{cn}^i is then computed as

$$f_{\text{cn}}^i = \sum_i^N \sum_{j \neq i}^N \left[1 + e^{-k_1(k_2(R_i^{\text{cov}} + R_j^{\text{cov}})/r_{ij} - 1)} \right]^{-1}, \quad (4.8)$$

where R_i^{cov} and R_j^{cov} are the scaled covalent radius of the i -th and j -th atoms, respectively, r_{ij} is the distance between the i -th and j -th atoms, k_1 and k_2 are empirical parameters equal to 16.0 and 4.0/3.0, respectively [146].

In the case of fluctuating charges and dipoles, the normalized Gaussian charge distribution

$$G(\mathbf{r}; \mathbf{C}) = \left(\frac{a}{\pi}\right)^{3/2} \exp[-a(\mathbf{r} - \mathbf{C})^2] \quad (4.9)$$

used in the DIM and cd-DIM models can be replaced with the coordination number dependent Gaussian charge distribution

$$G(\mathbf{r}; f_{cn}, \mathbf{C}) = \left(\frac{a_{cn}}{\pi}\right)^{3/2} \exp[-a_{cn}(\mathbf{r} - \mathbf{C})^2] \text{ with } a_{cn} = a(1 + bf_{cn}) . \quad (4.10)$$

The coordination number dependent dipoles are obtained from coordination dependent Gaussian charges by taking its gradient i.e. $\mu(\mathbf{r}; f_{cn}, \mathbf{C}) = -\nabla_{\mathbf{r}} G(\mathbf{r}; f_{cn}, \mathbf{C})$. Here, a is the fixed exponent of Gaussian charge distribution centred on atom with position vector \mathbf{C} , b is the coordination number scaling factor, which defines the coordination number dependent spread of the Gaussian charge distribution.

4.1.2 Parametrization of extended discrete interaction model for silver

In paper **V**, I adopt a scheme based on the concept of plasmon length [147]. The parametrization of the self-interaction tensors, \mathbf{c}_{ii} and $\boldsymbol{\alpha}_{ii}$, in ex-DIM is central since these tensors play the dominant role in defining the behavior of the polarizability of the NPs. Furthermore, in the case of dynamic polarizabilities, the frequency dependence is solely defined by these tensors. Similarly to DIM and cd-DIM, I use in ex-DIM a diagonal isotropic form for the self-interaction tensors, i.e. $\mathbf{c}_{ii,kl} = \delta_{kl}c$ and $\boldsymbol{\alpha}_{ii,kl} = \delta_{kl}\alpha$ for $k, l = x, y, z$. Here, I employed a different strategy based on the plasmon length [147] to parametrize the \mathbf{c}_{ii} and $\boldsymbol{\alpha}_{ii}$ tensors. Starting from the self-interaction tensor via the Clausius-Mossotti relationship for a spherical NP:

$$\boldsymbol{\alpha}_{ii,kl}(\omega) = \delta_{kl}f_{\alpha} \text{ with } f_{\alpha} = \frac{6}{\pi} R_i^3 \frac{\varepsilon(\omega) - \varepsilon_0}{\varepsilon(\omega) + 2\varepsilon_0}, \quad (4.11)$$

where R_i is the radius of the i -th atom, $\varepsilon(\omega)$ is the frequency dependent dielectric constant of the material, and ε_0 is the dielectric constant of the environment. In DIM [148] Eq. (4.11) is approximated as

$$\alpha_{ii,kl}(\omega = 0) = \alpha_{i,s,kl}, \quad (4.12)$$

$$\alpha_{ii,kl}(\omega > 0) = \alpha_{i,s,kl}(L_1(\omega) + L_2(\omega, N)), \quad (4.13)$$

where $\alpha_{i,s,kl}$ is the static polarizability and $L_1(\omega)$ and $L_2(\omega, N)$ are two separately normalized frequency dependent Lorentzians. The resonance frequency $\omega_{i,2}(N)$ in $L_2(\omega, N)$ is size-dependent

$$\omega_{i,2}(N) = \omega_{i,2}(1 + A/N^{1/3}), \quad (4.14)$$

where N is the total number of atoms and $\omega_{i,2}$ and A two fitted parameters. In this way the size-dependent frequency is inversely proportional to the radius for a spherical NP. The problems here are the discontinuity going from the static to the dynamic case due to the separately normalized Lorentzians and that the size dependent resonance frequency in $L_2(\omega, N)$ does not take into account the geometry of the NP. The cd-DIM [138] modifies the radius of Eq. (4.11) to a coordination number dependent radius $R_i(f_{cn})$ and dielectric constant $\varepsilon(\omega, f_{cn}, r)$

$$\alpha_{ii,kl}(\omega) = \delta_{kl} f_\alpha \text{ with } f_\alpha = \frac{6}{\pi} R_i^3(f_{cn}) \frac{\varepsilon(\omega, f_{cn}, r) - \varepsilon_0}{\varepsilon(\omega, f_{cn}, r) + 2\varepsilon_0}. \quad (4.15)$$

Here $\varepsilon(\omega, f_{cn}, r)$ is described by the sum of a the experimental dielectric constant ε_{exp} , a size-dependent Drude equation minus the Drude function for spherical NP:

$$\varepsilon(\omega, f_{cn}, r) = \varepsilon_{exp} + \varepsilon_{Drude}^{size}(\omega, f_{cn}, r) - \varepsilon_{Drude}(\omega), \quad (4.16)$$

where the the plasma frequency in the size dependent Drude function is modified by the coordination number. By using an effective coordination number there is a smooth transition from the inside to the outside of the coordination sphere. Both the DIM and cd-DIM should be able to describe the size dependence of spherical and spherical-like NP if properly parametrized. For shapes far from spherical symmetry, like nanorods with a large aspect ratio, the functional shape in the DIM and cd-DIM does not appear to be appropriate. This motivated me to develop a method which can take into account both the surface effects and geometry effects of nano clusters. In Ex-DIM

$$\alpha_{ii,kl}(\omega) = \left(\frac{R_i(f_{cn})}{R_{i,bulk}} \right)^3 \alpha_{i,s,kl} L(\omega, \mathbf{P}) \quad (4.17)$$

is the static polarizability $\alpha_{i,s,kl}$ [149] multiplied by a normalized Lorentzian $L(\omega, \mathbf{P})$ and the relative shift in radius from the bulk radius is determined by the coordination number. In this parameterization scheme, the chemical environment enters the definition of the α_{ii} tensor via $R_i(f_{cn})$ defined as

$$R_i(f_{cn}) = r_1 \left(1 - \frac{f_{cn}}{12}\right) + r_2 \frac{f_{cn}}{12}, \quad (4.18)$$

which regulates the radii of the atom depending on the coordination number. For Ag I use $r_1 = 1.65 \text{ \AA}$ and $r_2 = R_{i,bulk} = 1.56 \text{ \AA}$ which are the surface and bulk radii, respectively [138]. $L(\omega, \mathbf{P})$ regulates the geometric dependence via the size dependent resonance frequencies of three size-dependent Lorentzian oscillators

$$L(\omega, \mathbf{P}) = N(L_x(\omega, P_x) + L_y(\omega, P_y) + L_z(\omega, P_z)), \quad (4.19)$$

where each $L_i(\omega, P_i)$ depends on the plasmon length P_i in the i -th direction and the frequency ω with the common normalization factor N ensures that the Lorentzian oscillators are normalized in the static limit of $\omega = 0$. With a size-dependent Lorentzian oscillator in each direction it is possible to describe more complicated geometric structures with multiple plasmon resonances without having a new functional dependence for each distinct geometry and thereby make the ex-DIM more universal. The Lorentzian oscillator is chosen as

$$L_i = \frac{1}{\omega_i^2(P_i) - \omega^2 - i\gamma\omega}, \quad (4.20)$$

where γ describes the broadening of the spectra and $\omega_i(P_i)$ is the size-dependent resonance frequency which enables the geometric description of the plasmon excitations. With the choice of Lorentzian oscillator in Eq. (4.20) the normalization constant becomes

$$N = \left(\frac{1}{\omega_x^2(P_x)} + \frac{1}{\omega_y^2(P_y)} + \frac{1}{\omega_z^2(P_z)} \right)^{-1}. \quad (4.21)$$

The choice of Lorentzian oscillator in Eq. (4.20) and the common normalization in Eq. (4.21) will in this way give the higher peak for the lower incident frequency which, for nanorods, corresponds to the long side. The size-dependent resonance frequency $\omega_i(P_i)$ can be written as

$$\omega_i(P_i) = \omega_a(1 + A \cdot f(N, i)), \quad (4.22)$$

where ω_a and A are atom specific fitted parameters for the bulk resonance and size-dependence while $f(N, i)$ is a function of the number of atoms and dimension along the i -th direction measured in units of atom i . $f(N, i)$ must then in the bulk and atomic limits fulfil

$$\lim_{N, i \rightarrow \infty} f(N, i) = 0 \quad \lim_{N, i \rightarrow 1} f(N, i) = 1, \quad (4.23)$$

which can easily be accomplished using a single parameter namely the plasmon length P_i

$$f(N, i) = \frac{1}{P_i}, \quad (4.24)$$

where the plasmon length P_i is defined as the maximum distance between any atoms along the i -th direction plus the radius of each of the end point atoms. This use of the plasmon length is consistent with the experimental work from Tiggesbäumker *et al.* [150]. One can notice that the SPR cannot be directly proportional to the plasmon length as defined by Ringe *et al.* [147] since in the bulk limit the SPR would tend to minus infinity. Performing a Taylor expansion of Eq. (4.24) the first order is linear in the plasmon length and therefore the linear dependence on the plasmon length as observed by Ringe *et al.* [147] is consistent with a sample of clusters of a limited size range. For spherical clusters Eq. (4.24) reduces to the usual size dependence for classical models, also seen in the DIM and cd-DIM, but for rods, discs and other shapes far from spherical there is a distinct difference where the ex-DIM can have up to three distinct plasmon resonances.

The \mathbf{c}_{ii} tensor responsible for the self interaction energy in charge transfer processes is in the DIM modelled as

$$c_i(\omega) = c_{i,s} L_1(\omega) \quad (4.25)$$

using the same size-independent Lorentzian as in Eq. (4.13) for the polarizability in the DIM and a fitted parameter $c_{i,s}$ for the "static atomic capacitance". In the cd-DIM the charges and hence charge transfer and capacitance is completely removed. In the ex-DIM model I adopt a simplified two parameter scheme:

$$c_{ii,kl} = \delta_{kl} f_c \text{ with } f_c = c_{i,s} \left[1 + d \frac{R_i(f_{cn})}{R_i(12)} \right] L(\omega, \mathbf{P}), \quad (4.26)$$

where c is the "static atomic capacitance" parameter, similar by its physical origin to the capacitance used in DIM, d is a scaling factor for the coordination number dependence of

the capacitance, set to 0.1, and $L(\omega, \mathbf{P})$ is the Lorentzian oscillator defined in Eq. (4.19). Here, I stress that in our parameterization of the \mathbf{c}_{ii} tensor the frequency dependence is exactly the same as for the polarizability.

To reduce the number of parameters needed to be fitted and make the method easier to extend to other elements I make use of experimental or theoretical literature values or make argued choices for parameters which affect the peak position of the SPRs. The polarizabilities α are taken from the Schwerdtfeger and Nagle collection [149] which for silver is 55 au. The value of the capacitance parameter c , as I will show later, has very little influence on the overall polarizability and peak position as long as c is outside areas of numerical instability. For the optimization of spherical like clusters I have fixed the value at 0.0001 au since all systems appear to be numerically stable with this choice.

The Lorentzian broadenings γ should be small compared to the incident frequency and, not surprisingly, they show no significant influence on the position of the SPR. During the optimization γ has been fixed at 0.016 au which gives a reasonable broadening of the peak(s) with an full width at half maximum compared to that extrapolated from the Ringe *et al.* data. [147] While the SPR(s) does not shift with γ , except when two close lying double peaks merge, the width and height of the SPR(s) are significantly influenced thereby making it difficult to get a good set of parameters when optimized together with α for a small set of small clusters. Despite being optimized with $\gamma = 0.016$ it is no problem to adjust this parameter later or to make γ size dependent to obtain different peak heights since the placement of the SPR(s) is not affected by small changes in γ .

The only parameters that need to be fitted are therefore the size-dependent resonance frequency ω_a and the size-dependence factor A . Systematic investigations, like the one performed by Scholl *et al.* [151], are therefore essential for an accurate fit of ω_a and A . By plotting the energy of the SPR as a function of the inverse plasmon length I can fit the a simple linear function as shown in Fig. 4.1. From the fit in Fig. 4.1 the bulk limit for the SPR for Ag will be 3.25eV in our model and show a slow variation of the SPR as a function of the inverse plasmon length. With the definition of the plasmon length in Eq. (4.24) the inverse plasmon length cannot exceed the inverse diameter of an atom and the SPR is therefore finite.

By choosing a representative set of spherical clusters with a plasmon length of 1.4 – 3.8 nm an optimal resonance frequency, $\omega_i(P_i)$ in Eq. (4.22), which exactly reproduces the SPR from the fit in Fig. 4.1 for every cluster can be found. The optimal resonance frequency is here reproduced with a deviation of $10^{-6} - 10^{-5}$ of the SPR compared to experiment. Here I use several spherical cluster with the same plasmon length but with different surface topology to simulate slightly different surfaces. So while the radius in the $N = 459, 555$ and

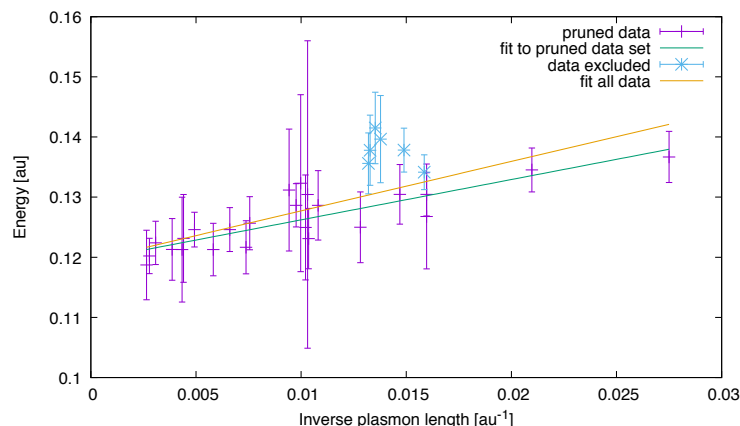


Figure 4.1: Linear fit ($a \cdot x + b$) of experimental data with error bars from Scholl *et al.* [151]. The purple points are the pruned data and green line the fit of the pruned data with coefficients $a = 0.671 \pm 0.059$ and $b = 0.119 \pm 0.001$. The blue points are data excluded from the pruning and the orange line a fit of all data with coefficients $a = 0.822 \pm 0.106$ and $b = 0.119 \pm 0.001$. Image taken from Paper V. Copyright 2019 American Chemical Society.

603 atoms clusters are the same the number of atoms and the surface topology are not. I find $\omega_a = 0.0794$ au and $A = 9.41$ au.

Inserting the fitted ω_a - and A -values and recalculating the clusters from the fit along with a test set of larger clusters with 276 – 11849 atoms and 2 – 7 nm radius make it possible to reproduce the SPR from the fit of the experimental values as seen in Fig. 4.3.

As seen from Fig. 4.3 I can reproduce the SPR of any spherical like cluster irrespectively of size with an error limited by the experimental error. To ensure that the behaviour of the polarizability is correct for all frequencies I calculated the polarizability dependent frequency for 200 points in the 3.0 – 4.6 eV region.

4.2 Results

4.2.1 Polarizability of spherical silver nanoparticles

Since DIM, cd-DIM and ex-DIM models have been applied to bare spherical-like silver clusters it would be natural to compare them to the experimental data since cd-DIM has been compared to the same data before [138] and ex-DIM is parameterized from the experimental data. The extracted data from the DIM and cd-DIM models have therefore been plotted

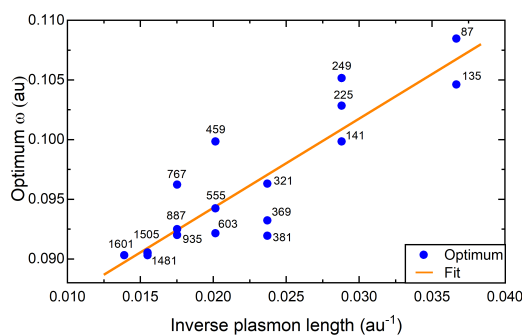


Figure 4.2: The optimum ($\omega_i(P_i)$) which reproduces the plasmon peak at the fitted experimental values from Fig. 4.1 for a given cluster. Fitting the optimum ($\omega_i(P_i)$) to Eq. (4.22) I find $\omega_a = 0.0794$ au and $A = 9.41$ au. The 1409 and 1433 atom clusters, also included in the fit, are located between or underneath the 1481 and 1505 atom clusters. Image taken from Paper V. Copyright 2019 American Chemical Society.

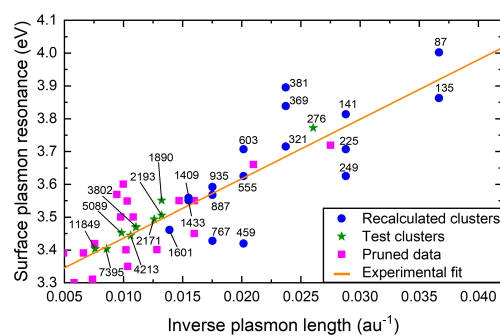


Figure 4.3: The plasmon peak as a function of the inverse plasmon length for the clusters used for the fit in Fig. 4.2 and a test set with larger clusters calculated with the fitted ω_a - and A -values compared to the experimental fit and pruned data. The 1481 and 1505 atoms recalculated clusters are located between or underneath the 1401 and 1433 atoms clusters. Image taken from Paper V. Copyright 2019 American Chemical Society.

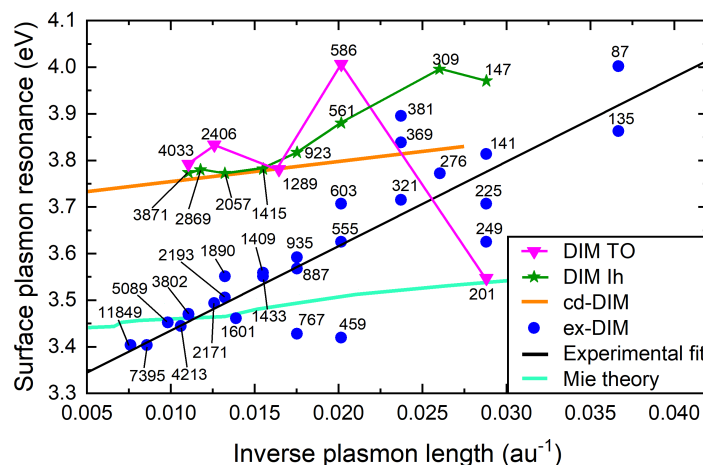


Figure 4.4: Comparison between the ex-DIM, DIM [148], cd-DIM [138] models and Mie theory and experiment for bare silver clusters[151]. For the DIM the TO clusters are truncated octahedrons and the Ih are icosahedral clusters. The diameter for the DIM clusters are estimated from the clusters used in the ex-DIM. The 1481 and 1505 atom recalculated clusters are located between or underneath the 1401 and 1433 atom clusters. Image taken from Paper V. Copyright 2019 American Chemical Society.

against experimental data and ex-DIM calculations as shown in Fig. 4.4. From the plotted data it is evident that for the truncated octahedrons the DIM model shows no discernible trend while for the icosahedra there is a red shift of around 0.2 eV with size but only for the range 147 – 1415 atoms (1.8 – 3.4 nm) thereafter there is no shift. The cd-DIM model does show a red shift in the plasmon length with increasing size but only by around 0.097 eV for the 2 – 10 nm clusters while the experimental data gives a red shift of 0.38 eV in that region. The limit of cd-DIM therefore deviates significantly from the experimental results and the results of ex-DIM. While Chen *et al.* [138] gives an arbitrary shift of 0.2 eV to the experimental data to compensate for solvent effects this does not change the fact that the shift in the SPR in the cd-DIM is only around a quarter of what it should be according to experiment [151].

The poor performance of the DIM and cd-DIM for spherical-like clusters is probably not due to methodological issues but rather due to the parameterization. This can be understood since ex-DIM and DIM in the spherical cases are very similar, except for the surface atoms, and a better fit of parameters should therefore be possible.

Mie theory [152] is known to be in good agreement with experiment for medium and large NPs, but not so for small NPs. As seen in Fig. 4.4 Mie theory underestimates the size

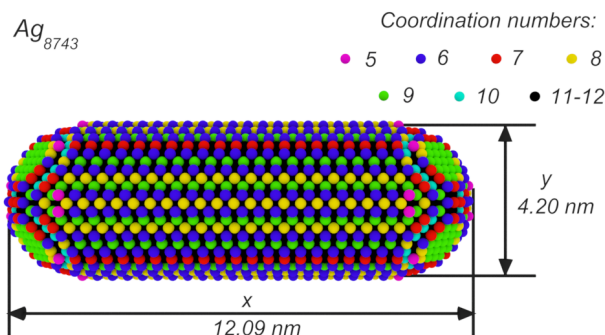


Figure 4.5: The scheme of longitudinal and transverse plasmon length and coordination numbers for the Ag nanorod with $N = 8743$ atoms which is 12.09 nm x 4.20 nm. Image taken from Paper V. Copyright 2019 American Chemical Society.

dependence of small silver clusters when compared to experiment even when Mie theory is size corrected based on the electron effective mean free path [66].

4.2.2 Polarizability of silver nanoparticles with complicated geometry: nanocubes and nanorods

As seen from Fig. 4.6 ex-DIM predict that the more acute size-dependence translate into a larger shape-dependence of the SPR as the Ag cubes are red shifted around 0.6 eV in comparison to the Ag spheres, in the region examined here, which is in line with the findings of González *et al.* [153]. The size-dependence of the cubes and spheres are here shown to be reasonably similar.

While a small red shift in the SPR with increasing cluster size is seen for spherical-like NP very significant red shifts can be observed for nanorods depending on the aspect ratio. This very large red shift can be used to tune the SPR to a given region, thereby making nanorods versatile sensors. The SPR for nanorods is, however, split into two due to the cylindrical symmetry and excitation of collective oscillations of conduction electrons of nanorods and two peaks are seen in the UV-vis spectrum. The TLSPR is typically very slightly blue shifted in comparison to the a spherical cluster with the same plasmon length while the LLSPR can be red shifted much below what can be done by increasing the size of a spherical cluster. Furthermore, the polarizability for the red shifted peak is also greatly enhanced with increasing aspect ratio, here defined as the ratio between the plasmon length in the longitudinal and transverse directions.

Since tunable nanorods are of great application interest I have examined a series of nanorods

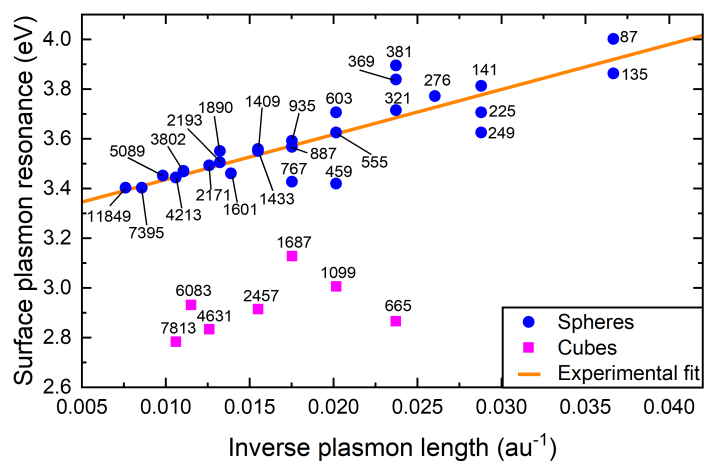


Figure 4.6: Comparison of the SPR for sphere and cubes with different plasmon lengths. The very red and blue shift seen for the 665 and 1687 atoms cubical clusters are due to double peaks where the most red and blue shifted peak, respectively has the highest polarizability. With a larger γ -value both outliers will be shifted more in line with the rest of the cubes. The 1481 and 1505 atom recalculated clusters are located between or underneath the 1401 and 1433 atom clusters. Image taken from Paper V. Copyright 2019 American Chemical Society.

to elucidate the interplay between the aspect ratio and diameter with respect to the SPR. I have constructed a series of nanorods where each end is a half sphere connected by a cylinder. The nanorods are designated as $Ag(x, y)$ where x is the plasmon length of the longitudinal axis and y is the plasmon length of the transverse axis in nm as shown in Fig. 4.5. $Ag(y, y)$ is, with this definition, a sphere with an effective diameter of y . Here I use nanorods with a diameter from 2.23 – 6.18 nm, a length up 14.06 nm, aspect ratio up to 5.4 and containing up to 16567 atoms. For all figures I calculate the polarizability at 400 different frequencies. In Fig. 4.5 it is clearly that only the top layer of atoms has a coordination number below 11 – 12 and, as expected, the atoms with the lowest coordination number are on the edges. This means that only the surface atoms are directly affected by the changes introduced by the coordination numbers. The red shift of the LLSPRs is clearly visible from Fig. 4.7 and furthermore the shift is directly proportional to the aspect ratio. The dependence on the diameter of the nanorod can also be seen. The increasing slope of the LLSPR with diameter is also observed for gold nanorods [154]. The slight blue shift of the TLSPR is observed as approximately linear. The experimental results *et al.* [155], in which the average width of the nanorods varies from 55 – 59 nm, indicate that the red shift is directly proportional to the aspect ratio and with a slight increase in slope compared to our results, which may be assigned to the refractive index in the surrounding medium. Here our results refers to nanorods on an ultra thin carbon film [151] while the experimental results were obtained in a 0.1M KNO_3 aqueous solution.

The relative polarizability and peak width between the LLSPR and TLSPR in Fig. 4.7 is seen to increase significantly with increasing aspect ratio. The polarizability per atom will also increase linearly with the aspect ratio. Both the LLSPR and the absorbance can in this way be controlled by the aspect ratio and the diameter of the nanorods. The polarizability thus depends substantially on the geometry of NP.

4.2.3 Plasmon resonances of hollow nanoparticles

I have applied the derived ex-DIM model also to hollow metallic nanospheres or nanoshells. These support plasmon resonances with frequencies that are sensitive functions of both the inner and outer radius of the metallic shell. For the specific case of nanoshells, the highly geometry-dependent plasmonic response can be seen as an interaction between the essentially fixed-frequency plasmon response of a nanosphere and that of a nanocavity. The sphere and cavity plasmons are electromagnetic excitations that induce surface charges at the inner and outer interfaces of the metal shell as shown on Fig. 4.9. Because of the finite thickness of the shell layer, the sphere and cavity plasmons interact with each other.

This interaction results in a splitting of the plasmon resonances into two new resonances:

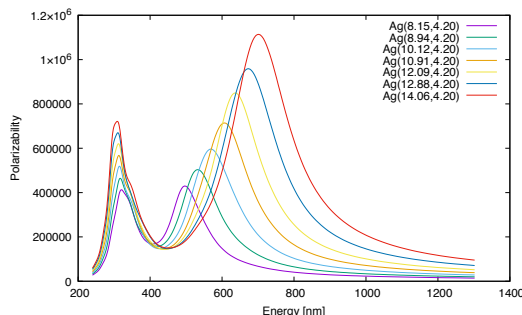


Figure 4.7: The polarizability as a function of the incident energy for $Ag(x, 4.20)$ nanorods with different longitudinal plasmon lengths. Image taken from Paper V. Copyright 2019 American Chemical Society.

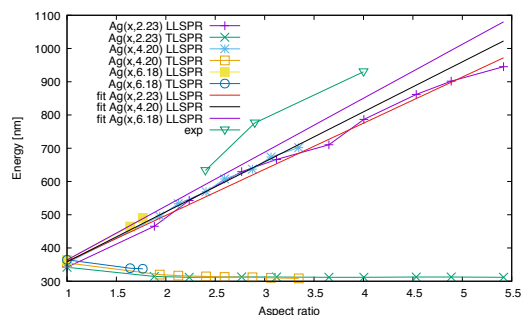


Figure 4.8: The LLSPR, TLSPR and fit of the LLSPR as a function of the aspect ratio for different nanorods. For the $Ag(x, 2.23)$ nanorods the TLSPR becomes a double peak and here only the right TLSPR is included. These are compared to the experimental LLSPR in a 0.1 M KNO_3 aqueous solution [155]. Image taken from Paper V. Copyright 2019 American Chemical Society.

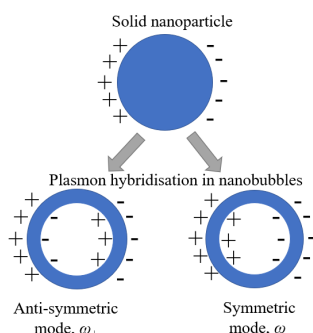


Figure 4.9: Scheme of existing modes in nanobubbles: symmetrical ω_- and anti-symmetrical ω_+ bondings. Image taken from Paper VII.

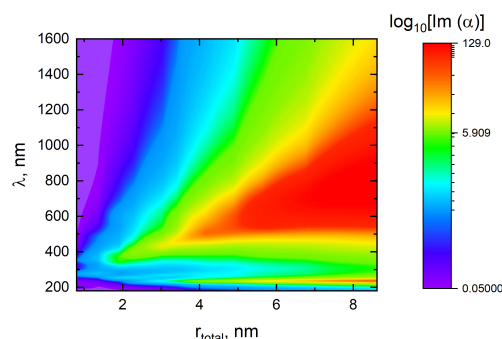


Figure 4.10: Logarithm of imaginary part of polarizability for set of nano-bubbles with fixed thickness of the shell (0.8 nm) and various total radius from 0.8 nm up to 8.6 nm. Image taken from Paper VII.

the lower energy symmetric or bonding plasmon and the higher energy antisymmetric or antibonding plasmon. The position of splitted plasmon modes with frequencies ω_- and ω_+ can be defined by following equation using the Drude model [156]:

$$\omega_{\pm}^2 = \frac{\omega_B^2}{2} \left[1 \pm \frac{1}{2l+1} \sqrt{1 + 4l(l+1) \left(\frac{r_{core}}{r_{total}} \right)^{2l+1}} \right], \quad (4.27)$$

where r_{core} and r_{total} are radius of core and total radius of particle, $\omega_{sphere} = \frac{\omega_B}{\sqrt{3}}$ correspond to position of resonance for solid spherical particle with same total radius, l is order of spherical harmonics ($l = 1$ in our case).

4.2.4 Polarizability of hollow nanoparticles

The studied nano-bubbles are presented as core-shell nanoparticles with an empty core inside. According to eq. (4.27) I can observe splitting of plasmon resonance into the two above mentioned resonances - the symmetrical bonding with ω_- and anti-symmetrical with ω_+ and can be expected to show red- and blue shifts correspondingly. The shift is dependent on both the total radius of the particle and the radius of the hole.

On Fig. 4.10 I show the spectral dependence for the imaginary part of the polarizability for the nano-bubbles with fixed thickness of the shell (1.6 nm) and different total radius r_{total} . Starting from solid (with $r_{hole} = 0$) spherical NP with $r_{total} = 0.8$, I increase the total size and size of hole simultaneously but keeping the shell thickness fixed at ≈ 0.8 nm, which corresponds to 3 atomic layers. When the size of the hole in the NP becomes bigger, the SPR of the solid NP becomes split into two resonances. One resonance shows a significant red shift with increasing r_{total} - from $\lambda = 400$ nm for $r_{total} = 2.5$ nm up to $\lambda = 900$ nm for $r_{total} = 8.4$ nm. This resonance corresponds to symmetrical "bonding", and its frequency is well described in eq. (4.27) as ω_- . It is clear that with increasing r_{total} I can see almost linear dependence for the position of the symmetric resonance vs. r_{total} . At the same time, as it was predicted in eq. (4.27), I'm able to show the second resonance at $\lambda = 218$ nm, corresponding to the anti-symmetrical mode with frequency ω_+ from eq. (4.27). This second resonance starts to appear at $r_{total} \approx 2.5$ nm. In contrast to the symmetrically bonded resonance, the anti-symmetrical one shows a very weak blue shift with increasing r_{total} .

4.3 Conclusions for Chapter 4

In this chapter I reviewed the extended discrete interaction model (ex-DIM) presented in my thesis, and demonstrated some simulations of the geometric and environmental dependence of plasmon nanoparticles (NPs). The frequency dependent dielectric function in this model is obtained from the Clausius-Mossotti relation as a sum of three Lorentzian oscillators and with Gaussian charge distributions and atomic radii that vary with the coordination number. The three frequency dependent Lorentzian oscillators depend on the plasmon length in the x, y, z - directions, with the so-called plasmon length[147].

I show both theoretically and numerically that the surface plasmon resonance (SPR) is inversely proportional to the plasmon length. I also show that the model can be parameterized from experiment with numerical accuracy of the same order as the experimental accuracy. In addition, I show that some parameters, such as broadening and capacitance, do not affect the position of the SPR peak to any noticeable extent, and that acceptable values for these parameters can be selected without adjustment.

Having parameterized the model for a set of spherical clusters, I used the model to predict the position of the plasmon resonance for a set of spherical clusters. To further demonstrate the capabilities of the ex-DIM model, I also performed a series of calculations on cubic and nanorod nanoparticles. For cubes, the SPRs turn up with a red shift compared to a spherical cluster with the same plasmon length. Nanorods show a significant red shift for the longitudinal resonance and a very weak blue shift for the transverse resonance with increasing aspect ratio. Having calculated several series of nanorods with different diameters and aspect radii, I could show that the red shift is directly proportional to the aspect ratio.

Next, I considered core-shell nanoparticles with an empty hole inside. I could demonstrate that our model can not only predict the shift of SPRs in such kind of particles, but also make it possible to get the correct positions of resonances in spectral ranges that are beyond the region where the model has been parametrized.

Chapter 5

Summary

The first part of the dissertation is devoted to the study of thermodynamic properties of plasmon nanostructures. The importance of taking into account the influence of temperature and the state of aggregation of a nanoparticle on its optical characteristics and *vice versa* was demonstrated. Subsequently, the method was used to model the optical and thermodynamic properties of chains of plasmon nanoparticles that can act as waveguides. It was shown that taking into account the thermal effects leads to a significant suppression in the waveguiding properties of such chains. One effective way to avoid the limitations associated with the deterioration of the waveguide properties of nanoparticles is to use heat-resistant materials. Titanium nitride was proposed as a refractory material. However, alternative plasmonic materials such as AZO, GZO and ITO can also be considered as promising materials for optical plasmon waveguides. Another possible way to prevent the negative influence of thermal suppression of plasmon resonances in chains of nanoparticles is to use a technological substrate that removes heat from the waveguide and save the nanoparticles from melting. These and many other technological solutions indicate that waveguides made of plasmonic nanoparticles are excellent candidates as a new generation of elements for integrated circuits.

In addition to the interest in microelectronics, plasmonics has great potential in many other fields. So, two-dimensional structures in the form of arrays of resonant nanoparticles are successfully used as filters and sensors with high sensitivity in biology and chemistry. The next part of the dissertation was devoted to the study of the optical properties of such two-dimensional structures from silicon nanoparticles. As being one of the most accessible and well-studied materials we have available, silicon opens up prospects for the production of high-tech devices with good reproducibility. However, defects in such devices can significantly reduce their versatility and increase the manufacturing costs. In this work, I simulated defects arising in two-dimensional structures from resonant silicon nanoparticles.

From the obtained results I was able to make the conclusion that two-dimensional structures might have high resistance to defects. In addition, such structures can be used as variable ultra-narrow-band filters. Theoretical research in this area is currently focused on using evolutionary mechanisms to create structures with predicted properties. Defects in two-dimensional structures can be used, if controlled, as a flexible way to create devices with completely new properties, such as focusing light. As highlighted in the previous chapter, new materials are one of the potentially interesting directions in the development of this area.

I consider all above reviewed applications to have a great technological value. However, research in these areas is limited to the methods used sometimes. In addition to the requirements for computing resources, most methods have a great fundamental limitation - the limited size and/or geometry of the structure. Here we are talking about the traditional difficulties of accurate modeling of properties of nanoparticles with sizes less than 10 nm and/or nanoparticles with an exotic (non-spherical) shape. In addition, most models rely on experimental data of the optical properties of nanoparticles and cannot predict their optical properties outside of existing experimental data. In this thesis, the model of discrete atomic interaction was expanded to remedy this situation. This model takes into account the contribution to the optical properties of nanoparticles from each atom. The obtained results for spherical nanoparticles, nanocubes and nanorods are in good general agreement with some theoretical predictions on larger particles made by other methods, for example, from the Mie theory. However, for the precise predictions of small nanoparticles can only be made by atomic discrete interaction models, of which our extended model constitutes the present state-of-art. Calculations were also performed for hollow nanoparticles. Since the model takes into account the contribution of each atom, it might be useful in studies of atomically thin nanostructures. Universal miniaturization invariably leads to the growing interest in modeling of nanoparticles with a certain number of atomic layers. The classical electrodynamics models do not allow to describe the optical properties of such structures. Also, the development of a discrete interaction model should consider new materials. Thus I believe the future is wide open both for applications of the current model and for its further development, with wide ramifications for applications already reviewed in this thesis, and for much more.

Bibliography

- [1] S. Zou, N. Janel, and G. C. Schatz, “Silver nanoparticle array structures that produce remarkably narrow plasmon lineshapes,” *The Journal of Chemical Physics*, vol. 120, no. 23, pp. 10871–10875, 2004.
- [2] S. Zou and G. C. Schatz, “Narrow plasmonic/photonic extinction and scattering line shapes for one and two dimensional silver nanoparticle arrays,” *The Journal of Chemical Physics*, vol. 121, no. 24, p. 12606, 2004.
- [3] V. A. Markel, “Divergence of dipole sums and the nature of non-Lorentzian exponentially narrow resonances in one-dimensional periodic arrays of nanospheres,” *Journal of Physics B: Atomic, Molecular and Optical Physics*, vol. 38, no. 7, pp. L115–L121, 2005.
- [4] R. Adato, A. A. Yanik, J. J. Amsden, D. L. Kaplan, F. G. Omenetto, M. K. Hong, S. Erramilli, and H. Altug, “Ultra-sensitive vibrational spectroscopy of protein monolayers with plasmonic nanoantenna arrays,” *Proceedings of the National Academy of Sciences*, vol. 106, no. 46, pp. 19227–19232, 2009.
- [5] Z. Li, S. Butun, and K. Aydin, “Ultranarrow Band Absorbers Based on Surface Lattice Resonances in Nanostructured Metal Surfaces,” *ACS Nano*, vol. 8, no. 8, pp. 8242–8248, 2014.
- [6] B. D. Thackray, V. G. Kravets, F. Schedin, G. Auton, P. A. Thomas, and A. N. Grigorenko, “Narrow Collective Plasmon Resonances in Nanostructure Arrays Observed at Normal Light Incidence for Simplified Sensing in Asymmetric Air and Water Environments,” *ACS Photonics*, vol. 1, no. 11, pp. 1116–1126, 2014.
- [7] R. R. Gutha, S. M. Sadeghi, and W. J. Wing, “Ultrahigh refractive index sensitivity and tunable polarization switching via infrared plasmonic lattice modes,” *Applied Physics Letters*, vol. 110, no. 15, p. 153103, 2017.

-
- [8] S. Zhou, X. Hunang, Q. Li, and Y. M. Xie, "Optimizing two-level hierarchical particles for thin-film solar cells," *Optics Express*, vol. 21, no. S2, p. A285, 2013.
- [9] G. Vecchi, V. Giannini, and J. Gómez Rivas, "Shaping the Fluorescent Emission by Lattice Resonances in Plasmonic Crystals of Nanoantennas," *Physical Review Letters*, vol. 102, no. 14, p. 146807, 2009.
- [10] F. Laux, N. Bonod, and D. Gérard, "Single Emitter Fluorescence Enhancement with Surface Lattice Resonances," *The Journal of Physical Chemistry C*, vol. 121, no. 24, pp. 13280–13289, 2017.
- [11] D. Khlopin, F. Laux, W. P. Wardley, J. Martin, G. A. Wurtz, J. Plain, N. Bonod, A. V. Zayats, W. Dickson, and D. Gérard, "Lattice modes and plasmonic linewidth engineering in gold and aluminum nanoparticle arrays," *Journal of the Optical Society of America B*, vol. 34, no. 3, p. 691, 2017.
- [12] Z.-S. Zhang, Z.-J. Yang, J.-B. Li, Z.-H. Hao, and Q.-Q. Wang, "Plasmonic interferences in two-dimensional stacked double-disk array," *Applied Physics Letters*, vol. 98, no. 17, p. 173111, 2011.
- [13] L. Lin and Y. Yi, "Orthogonal and parallel lattice plasmon resonance in core-shell SiO_2/Au nanocylinder arrays," *Optics Express*, vol. 23, no. 1, p. 130, 2015.
- [14] A. D. Humphrey and W. L. Barnes, "Plasmonic surface lattice resonances in arrays of metallic nanoparticle dimers," *Journal of Optics*, vol. 18, no. 3, p. 035005, 2016.
- [15] N. Mahi, G. Lévesque, O. Saison, J. Marae-Djouda, R. Caputo, A. Gontier, T. Maurer, P.-M. Adam, B. Bouhafs, and A. Akjouj, "In Depth Investigation of Lattice Plasmon Modes in Substrate-Supported Gratings of Metal Monomers and Dimers," *The Journal of Physical Chemistry C*, vol. 121, no. 4, pp. 2388–2401, 2017.
- [16] T. V. Teperik and A. Degiron, "Design strategies to tailor the narrow plasmon-photon resonances in arrays of metallic nanoparticles," *Physical Review B*, vol. 86, no. 24, p. 245425, 2012.
- [17] L.-H. Du, J. Li, Q. Liu, J.-H. Zhao, and L.-G. Zhu, "High-Q Fano-like resonance based on a symmetric dimer structure and its terahertz sensing application," *Opt. Mater. Express*, vol. 7, no. 4, p. 1335, 2017.
- [18] M. Hentschel, M. Saliba, R. Vogelgesang, H. Giessen, A. P. Alivisatos, and N. Liu, "Transition from Isolated to Collective Modes in Plasmonic Oligomers," *Nano Letters*, vol. 10, no. 7, pp. 2721–2726, 2010.

-
- [19] V. Grigoriev, S. Varault, G. Boudarham, B. Stout, J. Wenger, and N. Bonod, “Singular analysis of Fano resonances in plasmonic nanostructures,” *Physical Review A*, vol. 88, no. 6, p. 063805, 2013.
- [20] D. Wang, A. Yang, A. J. Hryn, G. C. Schatz, and T. W. Odom, “Superlattice Plasmons in Hierarchical Au Nanoparticle Arrays,” *ACS Photonics*, vol. 2, no. 12, pp. 1789–1794, 2015.
- [21] R. Nicolas, G. L  v  que, J. Mara  -Djouda, G. Montay, Y. Madi, J. Plain, Z. Herro, M. Kazan, P.-M. Adam, and T. Maurer, “Plasmonic mode interferences and Fano resonances in Metal-Insulator- Metal nanostructured interface,” *Scientific Reports*, vol. 5, no. 1, p. 14419, 2015.
- [22] R. Guo, T. K. Hakala, and P. T  rm  , “Geometry dependence of surface lattice resonances in plasmonic nanoparticle arrays,” *Physical Review B*, vol. 95, no. 15, p. 155423, 2017.
- [23] N. Kinsey, M. Ferrera, V. M. Shalaev, and A. Boltasseva, “Examining nanophotonics for integrated hybrid systems: a review of plasmonic interconnects and modulators using traditional and alternative materials [Invited],” *Journal of the Optical Society of America B*, vol. 32, no. 1, p. 121, 2015.
- [24] B. D. Thackray, P. A. Thomas, G. H. Auton, F. J. Rodriguez, O. P. Marshall, V. G. Kravets, and A. N. Grigorenko, “Super-Narrow, Extremely High Quality Collective Plasmon Resonances at Telecom Wavelengths and Their Application in a Hybrid Graphene-Plasmonic Modulator,” *Nano Letters*, vol. 15, no. 5, pp. 3519–3523, 2015.
- [25] P. A. Thomas, G. H. Auton, D. Kundys, A. N. Grigorenko, and V. G. Kravets, “Strong coupling of diffraction coupled plasmons and optical waveguide modes in gold stripe-dielectric nanostructures at telecom wavelengths,” *Scientific Reports*, vol. 7, no. 1, p. 45196, 2017.
- [26] M. E. Stewart, C. R. Anderton, L. B. Thompson, J. Maria, S. K. Gray, J. A. Rogers, and R. G. Nuzzo, “Nanostructured Plasmonic Sensors,” *Chemical Reviews*, vol. 108, no. 2, pp. 494–521, 2008.
- [27] K. Saha, S. S. Agasti, C. Kim, X. Li, and V. M. Rotello, “Gold Nanoparticles in Chemical and Biological Sensing,” *Chemical Reviews*, vol. 112, no. 5, pp. 2739–2779, 2012.

-
- [28] N. G. Khlebtsov, A. G. Melnikov, L. A. Dykman, and V. A. Bogatyrev, *Photopolarimetry in remote sensing*, ch. Optical properties and biomedical applications of nanostructures based on gold and silver bioconjugates, pp. 1–44. Kluwer Academic Pub., 2004.
- [29] C. Loo, L. Hirsch, M. Lee, E. Chang, I. West, N. Halas, and R. Drezek, “Gold nanoshell bioconjugates for molecular imaging in living cells,” *Optics Letters*, vol. 30, no. 9, pp. 1012–1014, 2005.
- [30] M. Stuart, “Phonemic analysis and reading development: some current issues,” *J. Res. Read.*, vol. 28, no. 1, pp. 39–49, 2005.
- [31] M. M. Cheng, G. Cuda, Y. L. Bunimovich, M. Gaspari, J. R. Heath, H. D. Hill, C. A. Mirkin, A. J. Nijdam, R. Terracciano, T. Thundat, and M. Ferrari, “Nanotechnologies for biomolecular detection and medical diagnostics,” *Current Opinion in Chemical Biology*, vol. 10, no. 1, pp. 11–19, 2006.
- [32] X. Huang, I. El-Sayed, W. Qian, and M. El-Sayed, “Cancer cell imaging and photothermal therapy in the near-infrared region by using gold nanorods,” *Journal of the American Chemical Society*, vol. 128, no. 6, pp. 2115–2120, 2006.
- [33] B. Khlebtsov, V. Zharov, A. Melnikov, V. Tuchin, and N. Khlebtsov, “Optical amplification of photothermal therapy with gold nanoparticles and nanoclusters,” *Nanotechnology*, vol. 17, no. 20, p. 5167, 2006.
- [34] J. Lakowicz, “Plasmonics in biology and plasmon-controlled fluorescence,” *Plasmonics*, vol. 1, no. 1, pp. 5–33, 2006.
- [35] G. Paciotti, D. Kingston, and T. L., “Colloidal gold nanoparticles: a novel nanoparticle platform for developing multifunctional tumor-targeted drug delivery vectors,” *Drug Development Research*, vol. 67, no. 1, pp. 47–54, 2006.
- [36] D. Pissuwan, S. Valenzuela, and M. Cortie, “Therapeutic possibilities of plasmonically heated gold nanoparticles,” *Trends Biotechnol.*, vol. 24, no. 2, pp. 62–67, 2006.
- [37] A. Wei, “Designing plasmonic nanomaterials as sensors of biochemical transport,” *e-Journal of Surface Science and Nanotechnology*, vol. 4, pp. 9–18, 2006.
- [38] P. Jain, I. El-Sayed, and M. El-Sayed, “Au nanoparticles target cancer,” *Nano Today*, vol. 2, no. 1, pp. 18–29, 2007.

-
- [39] B. N. Khlebtsov and N. G. Khelbtsov, “Biosensing potential of silica/gold nanoshells: Sensitivity of plasmon resonance to the local dielectric environment,” *J. Quant. Spectrosc. Radiat. Transfer*, vol. 106, no. 1-3, p. 154169, 2007.
 - [40] S. Kumar, N. Harrison, R. Richards-Kortum, and K. Sokolov, “Plasmonic nanosensors for imaging intracellular biomarkers in live cells,” *Nano Letters*, vol. 7, no. 5, pp. 1338–1343, 2007.
 - [41] N. Khlebtsov, “Optics and biophotonics of nanoparticles with a plasmon resonance,” *Quantum Electronics*, vol. 38, no. 6, pp. 504–529, 2008.
 - [42] M. Stewart, C. Anderton, L. Thompson, I. Maria, S. Gray, J. Rogers, and R. Nuzzo, “Nanostructured plasmonic sensors,” *Chemical Reviews*, vol. 108, no. 2, pp. 494–521, 2008.
 - [43] N. Khlebtsov and L. A. Dykman, “Optical properties and biomedical applications of plasmonic nanoparticles,” *J. Quant. Spectrosc. Radiat. Transfer*, vol. 111, no. 1, pp. 1–35, 2010.
 - [44] V. I. Zakomirnyi, I. L. Rasskazov, S. V. Karpov, and S. P. Polyutov, “New ideally absorbing Au plasmonic nanostructures for biomedical applications,” *J. Quant. Spectrosc. Radiat. Transf.*, vol. 187, pp. 54–61, 2017.
 - [45] A. S. Kostyukov, A. E. Ershov, V. S. Gerasimov, S. A. Filimonov, I. L. Rasskazov, and S. V. Karpov, “Super-efficient laser hyperthermia of malignant cells with core-shell nanoparticles based on alternative plasmonic materials,” *Journal of Quantitative Spectroscopy and Radiative Transfer*, vol. 236, p. 106599, 2019.
 - [46] U. Kreibig and M. Vollmer, *Optical Properties of Metal Clusters*. Berlin: Springer-Verlag, 1995.
 - [47] G. Shvets and I. Tsukerman, eds., *Plasmonics and plasmonic metamaterials. Analysis and applications*. Singapore: World Scientific, 2011.
 - [48] M. I. Stockman, “Nanoplasmonics: past, present, and glimpse into the future,” *Optics Express*, vol. 19, p. 22029, 2011.
 - [49] V. V. Klimov, *Nanoplasmonics*. Moscow: Fizmatlit, 2009.
 - [50] M. A. Garcia, “Surface plasmons in metallic nanoparticles: fundamentals and applications,” *Journal of Physics D: Applied Physics*, vol. 44, no. 28, p. 283001, 2011.

-
- [51] B. S. Luk'yanchuk, A. E. Miroshnichenko, M. I. Tribelsky, Y. S. Kivshar, and A. R. Khokhlov, "Paradoxes in laser heating of plasmonic nanoparticles," *New Journal of Physics*, vol. 14, no. 9, p. 093022, 2012.
- [52] G. Baffou, P. Berto, E. B. Urea, R. Quidant, S. Monneret, J. Polleux, and H. Rigneault, "Photoinduced heating of nanoparticle arrays," *ACS Nano*, vol. 7, no. 8, pp. 6478–6488, 2013.
- [53] A. D. Phan, T.-L. Phan, and L. M. Woods, "Near-field heat transfer between gold nanoparticle arrays," *Journal of Applied Physics*, vol. 114, no. 21, p. 214306, 2013.
- [54] A. P. Gavriluk and S. V. Karpov, "Processes in resonant domains of metal nanoparticle aggregates and optical nonlinearity of aggregates in pulsed laser fields," *Applied Physics B*, vol. 97, p. 163, 2009.
- [55] A. P. Gavriluk and S. V. Karpov, "Dynamic changes of optical characteristics of resonant domains in metal nanoparticle aggregates under pulsed laser fields," *Applied Physics B*, vol. 102, no. 1, pp. 65–72, 2010.
- [56] A. Ershov, A. Gavriluk, S. Karpov, and P. Semina, "Optodynamic phenomena in aggregates of polydisperse plasmonic nanoparticles," *Applied Physics B*, vol. 115, no. 4, pp. 547–560, 2014.
- [57] C. Kittel, *Introduction to Solid State Physics*. New York: John Wiley & Sons, Inc., 6th ed., 1986.
- [58] S. Hashimoto, D. Werner, and T. Uwada, "Studies on the interaction of pulsed lasers with plasmonic gold nanoparticles toward light manipulation, heat management, and nanofabrication," *Journal of Photochemistry and Photobiology C: Photochemistry Reviews*, vol. 13, no. 1, pp. 28 – 54, 2012.
- [59] V. A. Markel, L. S. Muratov, M. I. Stockman, and T. F. George, "Theory and numerical simulation of optical properties of fractal clusters," *Physical Review B*, vol. 43, no. 10, pp. 8183–8195, 1991.
- [60] B. T. Draine, "The discrete-dipole approximation and its application to interstellar graphite grains," *The Astrophysical Journal*, vol. 333, p. 848, 1988.
- [61] V. A. Markel, V. M. Shalaev, E. B. Stechel, W. Kim, and R. L. Armstrong, "Small-particle composites. i. linear optical properties," *Physical Review B*, vol. 53, no. 5, pp. 2425–2436, 1996.

-
- [62] C. F. Bohren and D. R. Huffman, *Absorption and Scattering of Light by Small Particles*. Weinheim, Germany: Wiley-VCH Verlag GmbH, 1998.
- [63] P. B. Johnson and R. W. Christy, “Optical constants of the noble metals,” *Physical Review B*, vol. 6, no. 12, pp. 4370–4379, 1972.
- [64] J. C. Miller, “Optical properties of liquid metals at high temperatures,” *Philosophical Magazine*, vol. 20, no. 168, pp. 1115–1132, 1969.
- [65] H. Zhou, I. Honma, and H. Komiyama, “Controlled synthesis and quantum-size effect in gold-coated nanoparticles,” *Physical Review B*, vol. 50, no. 16, p. 12052, 1994.
- [66] A. Moroz, “Electron Mean Free Path in a Spherical Shell Geometry,” *The Journal of Physical Chemistry C*, vol. 112, no. 29, pp. 10641–10652, 2008.
- [67] M. Otter, “Temperaturabhängigkeit der optischen konstanten massiver metalle,” *Zeitschrift für Physik*, vol. 161, no. 5, pp. 539–549, 1961.
- [68] M. V. Berry and I. C. Percival, “Optics of fractal clusters such as smoke,” *Optica Acta*, vol. 33, no. 5, pp. 577–591, 1986.
- [69] O. B. Wright, “Ultrafast nonequilibrium stress generation in gold and silver,” *Physical Review B*, vol. 49, pp. 9985–9988, 1994.
- [70] C.-K. Sun, F. Vallée, L. H. Acioli, E. P. Ippen, and J. G. Fujimoto, “Femtosecond-tunable measurement of electron thermalization in gold,” *Physical Review B*, vol. 50, pp. 15337–15348, 1994.
- [71] N. Del Fatti, C. Voisin, M. Achermann, S. Tzortzakis, D. Christofilos, and F. Vallée, “Nonequilibrium electron dynamics in noble metals,” *Physical Review B*, vol. 61, pp. 16956–16966, 2000.
- [72] R. H. M. Groeneveld, R. Sprik, and A. Lagendijk, “Femtosecond spectroscopy of electron-electron and electron-phonon energy relaxation in ag and au,” *Physical Review B*, vol. 51, pp. 11433–11445, 1995.
- [73] F. Claro and R. Rojas, “Novel laser induced interaction profiles in clusters of mesoscopic particles,” *Applied Physics Letters*, vol. 65, no. 21, pp. 2743–2745, 1994.
- [74] T. Castro, R. Reifengerger, E. Choi, and R. P. Andres, “Size-dependent melting temperature of individual nanometer-sized metallic clusters,” *Physical Review B*, vol. 42, pp. 8548–8556, 1990.

-
- [75] L. D. Landau, *Theory of elasticity*. Oxford England Burlington, MA: Butterworth-Heinemann, 1986.
- [76] V. A. Markel and A. K. Sarychev, "Propagation of surface plasmons in ordered and disordered chains of metal nanospheres," *Physical Review B*, vol. 75, p. 085426, 2007.
- [77] F. Ruting, "Plasmons in disordered nanoparticle chains: Localization and transport," *Physical Review B*, vol. 83, p. 115447, 2011.
- [78] I. L. Rasskazov, S. V. Karpov, and V. A. Markel, "Transmission and spectral properties of short optical plasmon waveguides," *Opt. Spectrosc.*, vol. 115, no. 5, pp. 666–674, 2013.
- [79] P. J. Compaijen, V. A. Malyshev, and J. Knoester, "Surface-mediated light transmission in metal nanoparticle chains," *Physical Review B*, vol. 87, no. 20, p. 205437, 2013.
- [80] I. L. Rasskazov, S. V. Karpov, G. Panasyuk, and V. A. Markel, "Overcoming the adverse effects of substrate on the waveguiding properties of plasmonic nanoparticle chains," *Journal of Applied Physics*, vol. 119, p. 043101, 2016.
- [81] W. C. Chew, *Waves and fields in inhomogeneous media*. New York: Van Nostrand Reinhold, 1990.
- [82] M. Paulus, P. Gay-Balmaz, and O. J. F. Martin, "Accurate and efficient computation of the greens tensor for stratified media," *Phys. Rev. E*, vol. 62, pp. 5797–5807, 2000.
- [83] G. Y. Panasyuk, J. C. Schotland, and V. A. Markel, "Short-distance expansion for the electromagnetic half-space green's tensor: general results and an application to radiative lifetime computations," *J. Phys. A*, vol. 42, no. 27, p. 275203, 2009.
- [84] W. H. Weber and G. W. Ford, "Propagation of optical excitations by dipolar interactions in metal nanoparticle chains," *Physical Review B*, vol. 70, no. 12, p. 125429, 2004.
- [85] B. Willingham and S. Link, "Energy transport in metal nanoparticle chains via sub-radiant plasmon modes," *Optics Express*, vol. 19, no. 7, p. 6450, 2011.
- [86] I. L. Rasskazov, S. V. Karpov, and V. A. Markel, "Waveguiding properties of short linear chains of nonspherical metal nanoparticles," *Journal of the Optical Society of America B*, vol. 31, no. 12, pp. 2981–2989, 2014.

-
- [87] I. L. Rasskazov, S. V. Karpov, and V. A. Markel, "Surface plasmon polaritons in curved chains of metal nanoparticles," *Physical Review B*, vol. 90, no. 7, p. 075405, 2014.
- [88] A. F. Koenderink and A. Polman, "Complex response and polariton-like dispersion splitting in periodic metal nanoparticle chains," *Physical Review B*, vol. 74, no. 3, p. 033402, 2006.
- [89] A. A. Govyadinov and V. A. Markel, "From slow to superluminal propagation: Dispersive properties of surface plasmon polaritons in linear chains of metallic nanospheroids," *Physical Review B*, vol. 78, no. 3, p. 035403, 2008.
- [90] I. B. Udagedara, I. D. Rukhlenko, and M. Premaratne, "Surface plasmon-polariton propagation in piecewise linear chains of composite nanospheres: The role of optical gain and chain layout," *Optics Express*, vol. 19, no. 21, p. 19973, 2011.
- [91] M. Conforti and M. Guasoni, "Dispersive properties of linear chains of lossy metal nanoparticles," *Journal of the Optical Society of America B*, vol. 27, no. 8, p. 1576, 2010.
- [92] M. Guasoni and M. Conforti, "Complex dispersion relation of a double chain of lossy metal nanoparticles," *Journal of the Optical Society of America B*, vol. 28, no. 5, p. 1019, 2011.
- [93] W. A. Jacak, "Exact solution for velocity of plasmon-polariton in metallic nano-chain," *Optics Express*, vol. 22, no. 16, p. 18958, 2014.
- [94] C. A. Downing, E. Mariani, and G. Weick, "Retardation effects on the dispersion and propagation of plasmons in metallic nanoparticle chains," *Journal of Physics: Condensed Matter*, vol. 30, no. 2, p. 025301, 2018.
- [95] P. J. Compaijen, V. A. Malyshev, and J. Knoester, "Time-dependent transport of a localized surface plasmon through a linear array of metal nanoparticles: Precursor and normal mode contributions," *Physical Review B*, vol. 97, no. 8, p. 085428, 2018.
- [96] K. H. Fung and C. T. Chan, "Plasmonic modes in periodic metal nanoparticle chains: a direct dynamic eigenmode analysis," *Optics Letters*, vol. 32, no. 8, p. 973, 2007.
- [97] P. J. Compaijen, V. A. Malyshev, and J. Knoester, "Engineering plasmon dispersion relations: hybrid nanoparticle chain -substrate plasmon polaritons," *Optics Express*, vol. 23, no. 3, p. 2280, 2015.

-
- [98] J. D. Jackson, *Classical electrodynamics*. John Wiley & Sons, Inc., 3rd ed., 1999.
- [99] A. Moroz, “Depolarization field of spheroidal particles,” *Journal of the Optical Society of America B*, vol. 26, no. 3, p. 517, 2009.
- [100] A. E. Ershov, V. S. Gerasimov, A. P. Gavriluk, S. V. Karpov, V. I. Zakomirnyi, I. L. Rasskazov, and S. P. Polyutov, “Thermal limiting effects in optical plasmonic waveguides,” *Journal of Quantitative Spectroscopy and Radiative Transfer*, vol. 191, pp. 1–6, 2017.
- [101] I. L. Rasskazov, S. V. Karpov, and V. A. Markel, “Nondecaying surface plasmon polaritons in linear chains of silver nanospheroids,” *Optics Letters*, vol. 38, no. 22, p. 4743, 2013.
- [102] S. A. Maier, P. G. Kik, H. A. Atwater, S. Meltzer, E. Harel, B. E. Koel, and A. A. Requicha, “Local detection of electromagnetic energy transport below the diffraction limit in metal nanoparticle plasmon waveguides,” *Nature Materials*, vol. 2, no. 4, pp. 229–232, 2003.
- [103] U. Guler, A. Boltasseva, and V. M. Shalaev, “Refractory Plasmonics,” *Science*, vol. 344, no. 6181, pp. 263–264, 2014.
- [104] V. S. Gerasimov, A. E. Ershov, S. V. Karpov, A. P. Gavriluk, V. I. Zakomirnyi, I. L. Rasskazov, H. Ågren, and S. P. Polyutov, “Thermal effects in systems of colloidal plasmonic nanoparticles in high-intensity pulsed laser fields [Invited],” *Optical Materials Express*, vol. 7, no. 2, p. 555, 2017.
- [105] N. Kinsey, M. Ferrera, G. V. Naik, V. E. Babicheva, V. M. Shalaev, and A. Boltasseva, “Experimental demonstration of titanium nitride plasmonic interconnects,” *Optics Express*, vol. 22, no. 10, p. 12238, 2014.
- [106] V. Zakomirnyi, I. Rasskazov, V. Gerasimov, A. Ershov, S. Polyutov, S. Karpov, and H. Ågren, “Titanium nitride nanoparticles as an alternative platform for plasmonic waveguides in the visible and telecommunication wavelength ranges,” *Photonics and Nanostructures: Fundamentals and Applications*, vol. 30, pp. 50–56, 2018.
- [107] J. C. Ndukaife, V. M. Shalaev, and A. Boltasseva, “Plasmonics - turning loss into gain,” *Science*, vol. 351, pp. 334–335, 2016.
- [108] G. W. Mulholland, C. F. Bohren, and K. A. Fuller, “Light Scattering by Agglomerates: Coupled Electric and Magnetic Dipole Method,” *Langmuir*, vol. 10, no. 8, pp. 2533–2546, 1994.

-
- [109] O. Merchiers, F. Moreno, F. González, and J. M. Saiz, “Light scattering by an ensemble of interacting dipolar particles with both electric and magnetic polarizabilities,” *Physical Review A - Atomic, Molecular, and Optical Physics*, vol. 76, no. 4, pp. 1–12, 2007.
- [110] A. B. Evlyukhin, C. Reinhardt, A. Seidel, B. S. Luk’Yanchuk, and B. N. Chichkov, “Optical response features of Si-nanoparticle arrays,” *Physical Review B - Condensed Matter and Materials Physics*, vol. 82, no. 4, pp. 1–12, 2010.
- [111] B. Auguié and W. L. Barnes, “Collective Resonances in Gold Nanoparticle Arrays,” *Physical Review Letters*, vol. 101, no. 14, p. 143902, 2008.
- [112] S. Rodriguez, M. Schaafsma, A. Berrier, and J. Gómez Rivas, “Collective resonances in plasmonic crystals: Size matters,” *Physica B: Condensed Matter*, vol. 407, no. 20, pp. 4081–4085, 2012.
- [113] A. García-Etxarri, R. Gómez-Medina, L. S. Froufe-Pérez, C. López, L. Chantada, F. Scheffold, J. Aizpurua, M. Nieto-Vesperinas, and J. J. Sáenz, “Strong magnetic response of submicron Silicon particles in the infrared,” *Optics Express*, vol. 19, no. 6, p. 4815, 2011.
- [114] D. Smirnova, A. I. Smirnov, and Y. S. Kivshar, “Multipolar second-harmonic generation by Mie-resonant dielectric nanoparticles,” *Physical Review A*, vol. 97, no. 1, p. 013807, 2018.
- [115] C. Zhang, Y. Xu, J. Liu, J. Li, J. Xiang, H. Li, J. Li, Q. Dai, S. Lan, and A. E. Miroshnichenko, “Lighting up silicon nanoparticles with Mie resonances,” *Nature Communications*, vol. 9, no. 1, p. 2964, 2018.
- [116] P. D. Terekhov, K. V. Baryshnikova, Y. A. Artemyev, A. Karabchevsky, A. S. Shalin, and A. B. Evlyukhin, “Multipolar response of nonspherical silicon nanoparticles in the visible and near-infrared spectral ranges,” *Physical Review B*, vol. 96, no. 3, p. 035443, 2017.
- [117] R. S. Savelev, A. P. Slobozhanyuk, A. E. Miroshnichenko, Y. S. Kivshar, and P. A. Belov, “Subwavelength waveguides composed of dielectric nanoparticles,” *Physical Review B*, vol. 89, no. 3, p. 035435, 2014.
- [118] V. E. Babicheva and A. B. Evlyukhin, “Resonant Lattice Kerker Effect in Metasurfaces With Electric and Magnetic Optical Responses,” *Laser & Photonics Reviews*, vol. 1700132, p. 1700132, 2017.

-
- [119] E. D. Palik, *Handbook of optical constants of solids II*. New York: Academic Press, 1998.
- [120] A. H. Schokker and A. F. Koenderink, “Statistics of Randomized Plasmonic Lattice Lasers,” *ACS Photonics*, vol. 2, no. 9, pp. 1289–1297, 2015.
- [121] A. H. Schokker and A. F. Koenderink, “Lasing in quasi-periodic and aperiodic plasmon lattices,” *Optica*, vol. 3, no. 7, p. 686, 2016.
- [122] L. Zundel and A. Manjavacas, “Finite-size effects on periodic arrays of nanostructures,” *Journal of Physics: Photonics*, vol. 1, no. 1, p. 015004, 2019.
- [123] J. R. Allardice and E. C. Le Ru, “Convergence of Mie theory series: criteria for far-field and near-field properties,” *Applied Optics*, vol. 53, no. 31, p. 7224, 2014.
- [124] J. Li, N. Verellen, and P. Van Dorpe, “Engineering electric and magnetic dipole coupling in arrays of dielectric nanoparticles,” *Journal of Applied Physics*, vol. 123, no. 8, p. 083101, 2018.
- [125] B. Augu  , X. M. Benda  a, W. L. Barnes, and F. J. Garc  a de Abajo, “Diffractive arrays of gold nanoparticles near an interface: Critical role of the substrate,” *Physical Review B*, vol. 82, no. 15, p. 155447, 2010.
- [126] Y. Chu, E. Schonbrun, T. Yang, and K. B. Crozier, “Experimental observation of narrow surface plasmon resonances in gold nanoparticle arrays,” *Applied Physics Letters*, vol. 93, no. 18, p. 181108, 2008.
- [127] R. C. Ng, J. C. Garcia, J. R. Greer, and K. T. Fountaine, “Polarization-independent, narrowband, near-IR spectral filters via guided mode resonances in ultrathin a-Si nanopillar arrays,” *ACS Photonics*, vol. 6, no. 2, pp. 265–271, 2019.
- [128] V. Gerasimov, A. Ershov, R. Bikbaev, I. Rasskazov, I. Timofeev, S. Polyutov, and S. Karpov, “Engineering mode hybridization in regular arrays of plasmonic nanoparticles embedded in 1d photonic crystal,” *Journal of Quantitative Spectroscopy and Radiative Transfer*, vol. 224, pp. 303–308, 2019.
- [129] V. S. Gerasimov, A. E. Ershov, A. P. Gavriluk, S. V. Karpov, H.   gren, and S. P. Polyutov, “Suppression of surface plasmon resonance in Au nanoparticles upon transition to the liquid state,” *Optics Express*, vol. 24, no. 23, pp. 26851–26856, 2016.
- [130] A. E. Ershov, V. S. Gerasimov, A. P. Gavriluk, and S. V. Karpov, “Surface plasmon resonances in liquid metal nanoparticles,” *Applied Physics B*, vol. 123, no. 6, p. 182, 2017.

-
- [131] V. I. Zakomirnyi, I. L. Rasskazov, V. S. Gerasimov, A. E. Ershov, S. P. Polyutov, and S. V. Karpov, "Refractory titanium nitride two-dimensional structures with extremely narrow surface lattice resonances at telecommunication wavelengths," *Applied Physics Letters*, vol. 111, no. 12, p. 123107, 2017.
- [132] V. I. Zakomirnyi, S. V. Karpov, H. Ågren, and I. L. Rasskazov, "Collective lattice resonances in disordered and quasi-random all-dielectric metasurfaces," *Journal of the Optical Society of America B*, vol. 36, no. 7, p. E21, 2019.
- [133] D. G. Baranov, D. A. Zuev, S. I. Lepeshov, O. V. Kotov, A. E. Krasnok, A. B. Evlyukhin, and B. N. Chichkov, "All-dielectric nanophotonics: the quest for better materials and fabrication techniques," *Optica*, vol. 4, no. 7, p. 814, 2017.
- [134] L. Jensen, P.-O. Åstrand, K. O. Sylvester-Hvid, and K. V. Mikkelsen, "Frequency-Dependent Molecular Polarizability Calculated within an Interaction Model," *The Journal of Physical Chemistry A*, vol. 104, no. 7, pp. 1563–1569, 2000.
- [135] L. L. Jensen and L. Jensen, "Electrostatic Interaction Model for the Calculation of the Polarizability of Large Noble Metal Nanoclusters," *The Journal of Physical Chemistry C*, vol. 112, no. 40, pp. 15697–15703, 2008.
- [136] V. I. Zakomirnyi, Z. Rinkevicius, G. V. Baryshnikov, L. K. Sørensen, and H. Ågren, "Extended Discrete Interaction Model: Plasmonic Excitations of Silver Nanoparticles," *The Journal of Physical Chemistry C*, p. acs.jpcc.9b07410, 2019.
- [137] A. Mayer, "Formulation in terms of normalized propagators of a charge-dipole model enabling the calculation of the polarization properties of fullerenes and carbon nanotubes," *Physical Review B*, vol. 75, p. 045407, 2007.
- [138] X. Chen, J. E. Moore, M. Zekarias, and L. Jensen, "Atomistic electrodynamics simulations of bare and ligand-coated nanoparticles in the quantum size regime," *Nature Communications*, vol. 6, p. 8921, 2015.
- [139] R. R. Birge, "Calculation of molecular polarizabilities using an anisotropic atom point dipole interaction model which includes the effect of electron repulsion," *The Journal of Chemical Physics*, vol. 72, no. 10, pp. 5312–5319, 1980.
- [140] B. Thole, "Molecular polarizabilities calculated with a modified dipole interaction," *Chem. Phys.*, vol. 59, no. 3, pp. 341–350, 1981.

-
- [141] L. Jensen, O. H. Schmidt, K. V. Mikkelsen, and P.-O. Åstrand, “Static and Frequency-Dependent Polarizability Tensors for Carbon Nanotubes,” *The Journal of Physical Chemistry B*, vol. 104, no. 45, pp. 10462–10466, 2000.
- [142] B. Shanker and J. Applequist, “Electronic absorption spectra of molecules and aggregates with interatomic charge transfer using a normal mode treatment of the atomic monopole-dipole interaction model,” *The Journal of Chemical Physics*, vol. 104, no. 16, pp. 6109–6116, 1996.
- [143] M. L. Olson and K. R. Sundberg, “An atom monopole-dipole interaction model with charge transfer for the treatment of polarizabilities of π -bonded molecules.,” *The Journal of Chemical Physics*, vol. 69, no. 12, pp. 5400–5404, 1978.
- [144] V. A. Markel, “Introduction to the Maxwell Garnett approximation: tutorial,” *J. Opt. Soc. Am. A*, vol. 33, no. 7, p. 1244, 2016.
- [145] S. Grimme, J. Antony, S. Ehrlich, and H. Krieg, “A consistent and accurate ab initio parametrization of density functional dispersion correction (DFT-D) for the 94 elements H-Pu,” *The Journal of Chemical Physics*, vol. 132, no. 15, p. 154104, 2010.
- [146] P. Pyykkö and M. Atsumi, “Molecular single-bond covalent radii for elements 1-118,” *Chem. - A Eur. J.*, vol. 15, no. 1, pp. 186–197, 2009.
- [147] E. Ringe, M. R. Langille, K. Sohn, J. Zhang, J. Huang, C. A. Mirkin, R. P. Van Duyne, and L. D. Marks, “Plasmon length: A universal parameter to describe size effects in gold nanoparticles,” *The Journal of Physical Chemistry Letters*, vol. 3, no. 11, pp. 1479–1483, 2012.
- [148] L. L. Jensen and L. Jensen, “Atomistic electrodynamics model for optical properties of silver nanoclusters,” *The Journal of Physical Chemistry C*, vol. 113, no. 34, pp. 15182–15190, 2009.
- [149] P. Schwerdtfeger and J. K. Nagle, “2018 table of static dipole polarizabilities of the neutral elements in the periodic table,” *Molecular Physics*, vol. 117, no. 9-12, pp. 1200–1225, 2019.
- [150] J. Tiggesbäumker, L. Köller, K.-H. Meiwes-Broer, and A. Liebsch, “Blue shift of the mie plasma frequency in ag clusters and particles,” *Physical Review A*, vol. 48, pp. R1749–R1752, 1993.
- [151] J. A. Scholl, A. L. Koh, and J. A. Dionne, “Quantum plasmon resonances of individual metallic nanoparticles,” *Nature*, vol. 483, no. 7390, pp. 421–427, 2012.

-
- [152] G. Mie, “Beiträge zur Optik trüber Medien, speziell kolloidaler Metallösungen,” *Ann. Phys.*, vol. 330, no. 3, pp. 377–445, 1908.
- [153] A. L. González, C. Noguez, J. Beránek, and A. S. Barnard, “Size, shape, stability, and color of plasmonic silver nanoparticles,” *The Journal of Physical Chemistry C*, vol. 118, no. 17, pp. 9128–9136, 2014.
- [154] L. S. Slaughter, W.-S. Chang, P. Swanglap, A. Tcherniak, B. P. Khanal, E. R. Zubarev, and S. Link, “Single-particle spectroscopy of gold nanorods beyond the quasi-static limit: Varying the width at constant aspect ratio,” *The Journal of Physical Chemistry C*, vol. 114, no. 11, pp. 4934–4938, 2010.
- [155] A. Jakab, C. Rosman, Y. Khalavka, J. Becker, A. Trügler, U. Hohenester, and C. Sönnichsen, “Highly sensitive plasmonic silver nanorods,” *ACS Nano*, vol. 5, no. 9, pp. 6880–6885, 2011.
- [156] E. Prodan, C. Radloff, N. Halas, and P. Nordlander, “A Hybridization Model for the Plasmon Response of Complex Nanostructures,” *Science*, vol. 302, no. 5644, pp. 419–422, 2003.